J. Fluid Mech. (2010), *vol.* 650, *pp.* 131–180.
doi:10.1017/S0022112009993557

Direct-simulation-based study of turbulent flow over various waving boundaries

DI YANG AND LIAN SHEN†

Department of Civil Engineering, Johns Hopkins University, Baltimore, MD 21218, USA

(Received 10 November 2008; revised 18 November 2009; accepted 18 November 2009; first published online 24 March 2010)

We use direct numerical simulation of stress-driven turbulent Couette flows over waving surfaces to study turbulence in the vicinity of water waves. Mechanistic study is performed through systematic investigation of different wavy surface conditions including plane progressive Airy and Stokes waves with and without wind-induced surface drift, as well as stationary wavy walls and vertically waving walls for comparison. Two different wave steepness values $ak = 0.1$ and 0.25 are considered, where a is the wave amplitude and k is the wavenumber. For effects of wave age, defined as the ratio between the wave phase speed c and the turbulence friction velocity u_*, we consider three values, namely $c/u_* = 2$, 14 and 25, corresponding to slow, intermediate and fast waves, respectively. Detailed analysis of turbulence structure and statistics shows their dependence on the above-mentioned parameters. Our result agrees with previous measurement and simulation results and reveals many new features unreported in the literature. Over progressive waves, although no apparent flow separation is found in mean flow, considerable intermittent separations in instantaneous flow are detected in slow waves with large steepness. The near-surface coherent vortical structures are examined. We propose two conceptual vortex structure models: quasi-streamwise and reversed horseshoe vortices for slow waves and bent quasi-streamwise vortices for intermediate and fast waves. Detailed examination of Reynolds stress with quadrant analysis, turbulent kinetic energy (TKE) and TKE budget with a focus on production shows large variation with wave phase; analysis shows that the variation is highly dependent on wave age and wave nonlinearity. Comparison between Airy waves and Stokes waves indicates that although the nonlinearity of surface water waves is a high-order effect compared with the wave age and wave steepness, it still makes an appreciable difference to the turbulence structure. The effect of wave nonlinearity on surface pressure distribution causes substantial difference in the wave growth rate. Wind-induced surface drift can cause a phase shift in the downstream direction and a reduction in turbulence intensity; this effect is appreciable for slow waves but negligible for intermediate and fast waves. In addition to providing detailed information on the turbulence field in the vicinity of wave surfaces, the results obtained in this study suggest the importance of including wave dynamics in the study of wind–wave interaction.

1. Introduction

Turbulent flow over a surface undergoing waving motion is of interest in many applications. Examples include wind–wave interaction at the sea surface (Miles 1957;

† Email address for correspondence: lianshen@jhu.edu

Lighthill 1962), drag reduction with a waving boundary undergoing fish-like motions (Taneda & Tomonari 1974; Triantafyllou, Triantafyllou & Yue 2000) and, in the limit of vanishing waving velocity, atmospheric flow over hills (Hunt, Leibovich & Richards 1988) and oceanic flow over sandbars (Zedler & Street 2001; Tseng & Ferziger 2004). Turbulent flow over a waving boundary differs substantially from that over a flat wall. In addition to the complex geometry associated with the wavy boundary (e.g. for wind over hills), the presence of the boundary waving motion (e.g. for wind over progressive waves and fish swimming) affects the flow field significantly. Wave boundary geometry and motion increase the complexity of the flow and the research associated with it.

Among the above applications, wind over waves is the focus of the current paper. The problem of wind–wave interaction is a challenging research topic of great importance. Prediction of the evolution of oceanic wave fields under wind forcing and modelling of atmosphere–ocean coupled systems requires a quantitative and fundamental understanding of the mechanism of wind–wave interaction. However, our current understanding of this problem is quite limited because of the complexity of the physics.

An early theoretical attempt by Jeffreys (1925) to explain the wind wave generation mechanism assumed that the air flow separation in the lee of the wave crest increases the form drag of the air and causes the wave to grow. This explanation, called the separated sheltering mechanism, was subsequently found to be inconsistent with the measurements of wind pressure over waves. In the 1950s, Phillips (1957) and Miles (1957) developed two wind wave growth theories. Phillips considered the generation of water waves by turbulent pressure fluctuations in the wind field. His theory employed a resonant mechanism and gave rise to a linear growth rate that is only effective for short waves at the initial stage of wind wave generation. Miles, on the other hand, applied a linear stability analysis to the shear flow over an infinitesimal water wave. He assumed the air flow to be inviscid, and turbulence was only considered to provide a mean shear profile. His result showed that the growth rate is determined by the flow around the 'critical layer', where the mean air flow velocity matches the phase velocity of the wave. Miles's mechanism predicts an exponential growth of water waves. Lighthill (1962) interpreted Miles's mechanism of wind input to surface waves as a 'vortex force' around the critical layer. Miles's critical-layer mechanism does not adequately describe wind over slow waves where the critical layer is very close to the wave surface or fast waves where the critical layer is distant from the wave surface and plays no significant role.

In recent years, the rapid distortion theory (RDT) has been successfully applied to the problem of wind–wave interaction. Belcher & Hunt (1993) considered the rapid distortion mechanism and applied a four-layer asymptotic model to the problem of shear flow over slowly moving waves. Cohen & Belcher (1999) later extended this work to flow over fast-moving waves. The non-separated sheltering mechanism from these studies complements Miles's critical-layer mechanism and provides a theoretical explanation for the growth of slow waves and the damping of fast waves under wind forcing.

In addition to the above-mentioned studies, there are also other important theoretical analyses on wind–wave interaction. For example, Fabrikant (1976) and Janssen (1982) developed a quasi-linear wind wave generation theory by tracking the wind profile evolution and applying Miles's theory at each particular time. This quasi-linear theory improved the prediction of wind wave growth. Makin,

Kudryavtsev & Mastenbroek (1995) developed a parametric-description-based wind-over-waves coupling (WOWC) theory that was later successfully applied to show the effects of various sea surface phenomena (e.g. wave breaking and long–short wave interaction) on wind–wave interaction (e.g. Makin & Kudryavtsev 2002; Makin *et al.* 2007).

In the past few decades, many field measurements have been performed in oceans and lakes to investigate the interaction between wind turbulence and surface water waves (see, among many others, Snyder *et al.* 1981; Hristov, Miller & Friehe 2003; Donelan *et al.* 2006). These measurements provide valuable information on the flow field, including mean velocity profile and air pressure distribution, that can be used to evaluate the energy input from wind to water waves. However, the detailed flow structure in the vicinity of the wave surface is difficult to obtain because of the complex environment in the field. To make accurate measurement, the probe needs to be close enough to the water surface (below the wave crests) but meanwhile needs to stay dry. Moreover, the wave-induced pressure and turbulence is small compared with the already-existing atmospheric turbulence. All these make the field measurement difficult. In a recent series of carefully designed wave-follower field measurements (Donelan *et al.* 2005, 2006; Babanin *et al.* 2007), detailed and extensive near-surface pressure data for strong wind over steep waves were obtained. These data provide valuable information for the validation of the current numerical result. Quantitative comparison is given in the present paper. Besides field measurements, more controlled laboratory experiments provide detailed information on the turbulence field. However, many of the laboratory experiments are for turbulence over stationary wavy boundaries (e.g. Hudson, Dykhno & Hanratty 1996; Nakagawa & Hanratty 2001; Günther & von Rohr 2003; Kruse, Günther & von Rohr 2003), and those for turbulence over water waves (e.g. Stewart 1970; Banner & Melville 1976; Hsu, Hsu & Street 1981; Hsu *et al.* 1982; Mastenbroek 1996; Donelan *et al.* 2004; Makin *et al.* 2007; Veron, Saxena & Misra 2007; Reul, Branger & Giovanangeli 2008; Shaikh & Siddiqui 2008; Donelan & Plant 2009) are more challenging because of the moving boundary.

In addition to theoretical and experimental study, numerical simulation has been a useful research tool. For example, Gent & Taylor (1976) applied a mixing-length model in their Reynolds-averaged Navier–Stokes (RANS) simulation of turbulence over water waves and showed that a varying surface roughness may significantly increase the energy input from turbulence to surface waves. Al-Zanaidi & Hui (1984) used a two-equation closure model and found that the rate of wave growth can be significantly different depending on if the turbulent flow is transitional, smooth or rough.

On the basis of the RDT, Belcher & Hunt (1993, 1998) showed that in the outer region of the flow, the turbulent eddies are advected too rapidly to transport significant momentum, so that the effect of shear stress perturbation on the mean flow calculation is negligible there. They pointed out that the erroneous application of the mixing-length model over the whole flow region in earlier RANS studies incorrectly models the stress gradients in the outer region, which affects the accuracy of the form drag calculation and results in inaccurate prediction of wave growth rate.

An important improvement in RANS simulation was made by Mastenbroek *et al.* (1996; see also Mastenbroek 1996), who obtained model and measurement results consistent with the RDT prediction and showed the importance of using the second-order Reynolds stress closure model, namely the Launder–Reece–Rodi (LRR) model. The

second-order model was later used in several other RANS simulations (e.g. Li, Xu & Taylor 2000; Meirink & Makin 2000).

With the above-mentioned progress in theoretical, experimental and numerical studies in the past five decades, the understanding of the physics of wind wave growth has been improved significantly. But there still exists about 50 % difference between the values of wave growth rate measured in the laboratories and field and the ones predicted by theories and models, especially for slow waves (cf. Mastenbroek 1996; Belcher & Hunt 1998). Recently, Peirson & Garcia (2008) showed that the discrepancy between model prediction and measurement can be reduced significantly if a wave-coherent tangential stress contribution is included in the calculation of growth rate.

Beyond RANS simulation, large-eddy simulation (LES) can resolve large-scale flow motions with the effects of small-scale motions represented by subgrid-scale models. Being able to directly address the unsteady flow structures that are inherent in the non-equilibrium turbulence field over the wavy boundary, LES appears promising. Gong, Taylor & Dörnbrack (1996), Henn & Sykes (1999), Zedler & Street (2001), Tseng & Ferziger (2004), Wan, Porté-Agel & Stoll (2007) and Sullivan *et al.* (2008) performed LES for turbulent flows over wavy surfaces. If a no-slip boundary condition is used on the wavy surface, the Reynolds number cannot be too large because the wall boundary layer needs to be resolved. For high Reynolds numbers to be considered, a wall-layer model is needed.

The accuracy of RANS simulation and LES is directly affected by the applicability of turbulence models in the complex problem of wind–wave interaction. With the continuous increase in computer power, direct numerical simulation (DNS) (cf. Moin & Mahesh 1998) has become feasible for simulating turbulence over wavy surfaces. At relatively low Reynolds numbers and without turbulence modelling, DNS provides detailed turbulence flow field data. Choi, Moin & Kim (1992), Krettenauer & Schumann (1992), Maass & Schumann (1994), De Angelis, Lombardi & Banerjee (1997), Cherukat *et al.* (1998), Sullivan, McWilliams & Moeng (2000), Shen *et al.* (2003) and Kihara *et al.* (2007) performed DNS for turbulence over various wavy boundaries. Results from these DNS provide useful information on different aspects of the dynamics of turbulence near a wavy boundary.

In the current study, we use DNS to perform a comprehensive study of turbulence over waving surfaces. The structures, statistics and dynamics of the flow are highly dependent on a wide range of factors including wave age, wave amplitude, wave nonlinearity and wind-induced surface drift. In the current work, we investigate the effects of the above-mentioned processes systematically in order to obtain a complete picture of the physical processes. Some of these processes were ignored in previous studies. For example, most previous DNS studies on turbulence over water waves considered only simple water wave boundary conditions with wave steepness small and wave nonlinearity ignored. In order to study the effect of surface wave nonlinearity on turbulence, we consider a Stokes wave with large steepness $ak = 0.25$. Comparison between Stokes and Airy waves allows us to quantify the influence of wave nonlinearity on the turbulence structures and dynamics, especially on the pressure-induced wave growth rate. We also consider the effect of wind-induced surface drift on turbulence, which is expected to be appreciable in slow waves, since the drift velocity may be comparable to the wave orbital velocity.

The extensive data on the three-dimensional, instantaneous flow field obtained in our DNS enable us to perform a comprehensive analysis of the structures and statistics of the turbulence in the vicinity of the wave surface. In the present paper, we

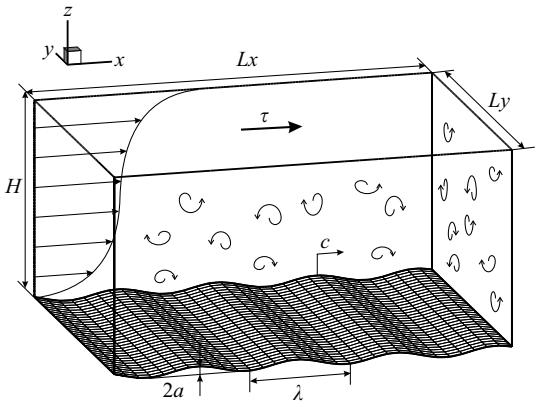

FIGURE 1. Sketch of a turbulent Couette flow over a wavy boundary. The flow is driven by a constant shear stress τ on the top boundary. The surface wave has a wavelength λ and an amplitude a. The wave propagates in the x-direction with a phase speed c.

present detailed results on turbulence statistics, including Reynolds stress, quadrant analysis and turbulent kinetic energy (TKE) budget with a focus on production. The instantaneous flow field is examined, with particular attention paid to the occurrence of intermittent flow separation. We also obtain well-resolved wave-coherent vortical structures. On the basis of the characteristics of these vortices and their dependence on surface wave motion, we propose a conceptual model for near-surface coherent vortical structures that explains the relation between Reynolds stress and coherent turbulent motions.

Besides the illustration of the fine turbulence structure, it is important for the DNS to capture the key quantifications of the wind–wave interaction problem. In the current study, the wave phase dependence and the vertical distribution of the pressure field are analysed and compared with the literature, and their variations with respect to wave steepness, wave age, wave nonlinearity and surface drift are studied. The wave form drag and growth rate are quantified, and their dependence on the wave conditions is investigated systematically. Extensive comparison and validation with existing field and lab measurements, numerical simulations and theoretical analyses are performed, and satisfying results are obtained.

This paper is organized as follows. The problem definition and numerical method are discussed in § 2. Section 3 shows the phase-averaged flow field. In § 4, the instantaneous flow structure is studied. Section 5 presents statistical turbulence quantities, including Reynolds stress, quadrant analysis and TKE budget with a focus on production. In § 6, the dependence of the pressure field and the consequent wave growth rate on the wave boundary condition is studied. Finally, a discussion and conclusions are provided in § 7.

2. Problem definition and numerical method

2.1. *Flow configuration and mathematical formulation*

We consider the three-dimensional turbulent Couette flow over a wavy boundary as shown in figure 1. In this canonical problem, the flow is driven by a constant shear stress τ at the top boundary. The shear stress is related to the turbulence friction velocity by $u_* = \sqrt{\tau/\rho}$, where ρ is the fluid density. The Cartesian frame is fixed

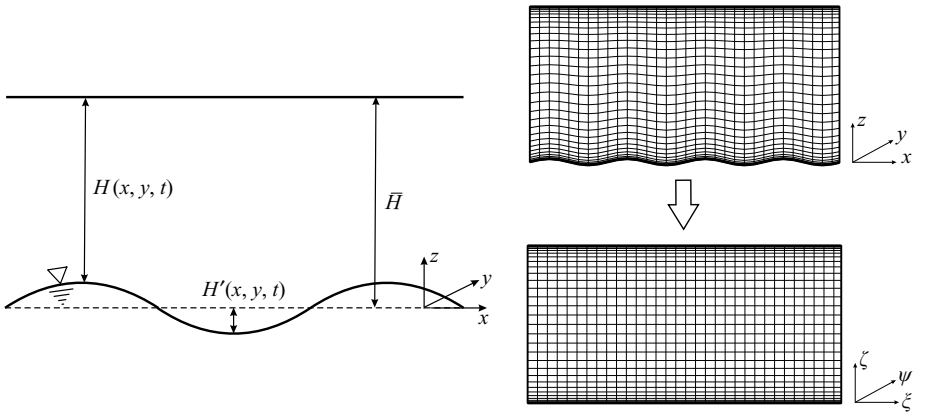

FIGURE 2. Illustration of coordinate transformation. The height of the physical domain H is decomposed into an average height $\overline{H}$ and a wave-induced variation H'. The irregular physical domain in the (x, y, z, t) space is transformed to a rectangular computational domain in the (ξ, ψ, ζ, τ) space by an algebraic mapping. Here only the mapping in the (x, z)-plane is shown. In the y-direction, the grid is uniform and is not plotted.

in space, with x, y and z being the streamwise, spanwise and vertical coordinates, respectively. Here a is the wave amplitude; λ is the wavelength; $k = 2\pi/\lambda$ is the wavenumber; and c is the wave phase speed. The surface wave motion is prescribed. The details of the wavy boundary condition are discussed in § 2.4. We note that although the prescribed wave is two-dimensional, which corresponds to the case of being uniform in the transverse direction, the turbulent flow above the wave is simulated in the three-dimensional frame. Therefore, the velocity obtained from our simulation has three components, u, v and w, which are functions of (x, y, z). For the phase-averaged statistics shown in the current paper, the results reduce to two-dimensional and are presented as functions of (x, z).

The turbulent flow motions are described by the incompressible Navier–Stokes equations

$$\rho\left(\frac{\partial u_i}{\partial t} + \frac{\partial u_i u_j}{\partial x_j}\right) = -\frac{\partial p}{\partial x_i} + \mu\frac{\partial^2 u_i}{\partial x_j \partial x_j}, \tag{2.1}$$

$$\frac{\partial u_i}{\partial x_i} = 0. \tag{2.2}$$

Here $u_i (i = 1, 2, 3) = (u, v, w)$; p is the pressure; and μ is the dynamic viscosity.

2.2. *Algebraic mapping*

A major difficulty in the simulation of flow over a wavy boundary is that the physical domain is non-rectangular and cannot be easily discretized by a regular Cartesian grid system. In our simulation, we use a boundary-fitted grid system that enables the direct simulation of the turbulent flow down to the wave surface with the boundary layer resolved. As shown in figure 2, the irregular wave-following physical space (x, y, z, t) is transformed to a rectangular computational space (ξ, ψ, ζ, τ) with the following algebraic mapping:

$$\tau = t, \quad \xi = x, \quad \psi = y, \quad \zeta = \frac{z + H'}{H' + \overline{H}}. \tag{2.3}$$

Here the height of the physical domain H is decomposed into an average height $\overline{H}$ and a wave-induced variation $H'(x, y, t)$. The origin of the z-axis in the physical space is set at the mean surface level, and the top boundary is at $z = \overline{H}$. This algebraic mapping, though seemingly simple in its form, is found to be highly efficient in our simulations of turbulent flows over nonlinear wave boundaries, e.g. high-order representation of Stokes waves.

Note that H' is a function of x, y and t. By applying the chain rule to partial differentiations, we obtain the following transformation of derivatives:

$$\left.\begin{aligned}
\frac{\partial}{\partial t} &= \frac{\partial}{\partial \tau} + \frac{H'_t - \zeta H'_t}{H' + \overline{H}} \frac{\partial}{\partial \zeta}, \\
\frac{\partial}{\partial x} &= \frac{\partial}{\partial \xi} + \frac{H'_x - \zeta H'_x}{H' + \overline{H}} \frac{\partial}{\partial \zeta}, \\
\frac{\partial}{\partial y} &= \frac{\partial}{\partial \psi} + \frac{H'_y - \zeta H'_y}{H' + \overline{H}} \frac{\partial}{\partial \zeta}, \\
\frac{\partial}{\partial z} &= \frac{1}{H' + \overline{H}} \frac{\partial}{\partial \zeta}.
\end{aligned}\right\} \tag{2.4}$$

By substituting operators (2.4) into (2.1) and (2.2), we obtain fully nonlinear governing equations in the computational space:

$$\rho \left(\frac{\partial u}{\partial \tau} + \frac{H'_t - \zeta H'_t}{H' + \overline{H}} \frac{\partial u}{\partial \zeta} + \frac{\partial (uu)}{\partial \xi} + \frac{H'_x - \zeta H'_x}{H' + \overline{H}} \frac{\partial (uu)}{\partial \zeta} + \frac{\partial (uv)}{\partial \psi} + \frac{H'_y - \zeta H'_y}{H' + \overline{H}} \frac{\partial (uv)}{\partial \zeta} + \frac{1}{H' + \overline{H}} \frac{\partial (uw)}{\partial \zeta} \right) = -\frac{\partial p}{\partial \xi} - \frac{H'_x - \zeta H'_x}{H' + \overline{H}} \frac{\partial p}{\partial \zeta} + \mu \nabla^2 u, \tag{2.5}$$

$$\rho \left(\frac{\partial v}{\partial \tau} + \frac{H'_t - \zeta H'_t}{H' + \overline{H}} \frac{\partial v}{\partial \zeta} + \frac{\partial (vu)}{\partial \xi} + \frac{H'_x - \zeta H'_x}{H' + \overline{H}} \frac{\partial (vu)}{\partial \zeta} + \frac{\partial (vv)}{\partial \psi} + \frac{H'_y - \zeta H'_y}{H' + \overline{H}} \frac{\partial (vv)}{\partial \zeta} + \frac{1}{H' + \overline{H}} \frac{\partial (vw)}{\partial \zeta} \right) = -\frac{\partial p}{\partial \psi} - \frac{H'_y - \zeta H'_y}{H' + \overline{H}} \frac{\partial p}{\partial \zeta} + \mu \nabla^2 v, \tag{2.6}$$

$$\rho \left(\frac{\partial w}{\partial \tau} + \frac{H'_t - \zeta H'_t}{H' + \overline{H}} \frac{\partial w}{\partial \zeta} + \frac{\partial (wu)}{\partial \xi} + \frac{H'_x - \zeta H'_x}{H' + \overline{H}} \frac{\partial (wu)}{\partial \zeta} + \frac{\partial (wv)}{\partial \psi} + \frac{H'_y - \zeta H'_y}{H' + \overline{H}} \frac{\partial (wv)}{\partial \zeta} + \frac{1}{H' + \overline{H}} \frac{\partial (ww)}{\partial \zeta} \right) = -\frac{1}{H' + \overline{H}} \frac{\partial p}{\partial \zeta} + \mu \nabla^2 w, \tag{2.7}$$

$$\frac{\partial u}{\partial \xi} + \frac{H'_x - \zeta H'_x}{H' + \overline{H}} \frac{\partial u}{\partial \zeta} + \frac{\partial v}{\partial \psi} + \frac{H'_y - \zeta H'_y}{H' + \overline{H}} \frac{\partial v}{\partial \zeta} + \frac{1}{H' + \overline{H}} \frac{\partial w}{\partial \zeta} = 0, \tag{2.8}$$

where the Laplacian operator is decomposed into $\nabla^2 = \nabla^2_{\xi\psi} + \nabla^2_{\zeta}$ as

$$\nabla^2_{\xi\psi} = \frac{\partial^2}{\partial \xi^2} + \frac{\partial^2}{\partial \psi^2} + 2 \frac{H'_x - \zeta H'_x}{H' + \overline{H}} \frac{\partial^2}{\partial \xi \partial \zeta} + 2 \frac{H'_y - \zeta H'_y}{H' + \overline{H}} \frac{\partial^2}{\partial \psi \partial \zeta}, \tag{2.9}$$

$$\nabla^2_{\zeta} = \left(\frac{(H'_{xx} + H'_{yy})(1 - \zeta)}{H' + \overline{H}} - 2 \frac{(H'^2_x + H'^2_y)(1 - \zeta)}{(H' + \overline{H})^2} \right) \frac{\partial}{\partial \zeta} + \frac{1 + (H'_x - \zeta H'_x)^2 + (H'_y - \zeta H'_y)^2}{(H' + \overline{H})^2} \frac{\partial^2}{\partial \zeta^2}. \tag{2.10}$$

2.3. Numerical scheme

For spatial discretization, we use a Fourier-series-based pseudo-spectral method in the horizontal directions. In the vertical direction, we use a second-order finite-difference scheme on a staggered grid (Harlow & Welch 1965; Shen *et al.* 2003). We use an evenly distributed grid with 128 points in both the streamwise and spanwise directions. In the vertical direction, we use 129 grid points that are clustered towards the bottom and top boundaries. The relatively small number of grid points compared with modern turbulence simulation in the rectangular domain is necessitated by the complexity associated with the wavy geometry and the extra terms and iteration in the nonlinear treatment, which substantially increases the computational cost.

The Navier–Stokes equations (2.1) and (2.2) are advanced in time by a fractional-step method of Kim & Moin (1985), which is modified here for this nonlinear problem:

$$\rho\left(\frac{\hat{u}_i - u_i^n}{\Delta t} + \frac{1}{2}\left(\left(\frac{H_t' - \zeta H_t'}{H' + \overline{H}}\right)^{n+1}\frac{\partial \hat{u}_i}{\partial \zeta} + \left(\frac{H_t' - \zeta H_t'}{H' + \overline{H}}\right)^{n}\frac{\partial u_i^n}{\partial \zeta}\right)\right) = \frac{1}{2}\left(3C_i^n - C_i^{n-1}\right) + \mu\nabla_\zeta^2\frac{(\hat{u}_i + u_i^n)}{2}, \quad (2.11)$$

$$\rho\left(\frac{u_i^{n+1} - \hat{u}_i}{\Delta t}\right) = -\frac{\partial \boldsymbol{\phi}}{\partial x_i}^{n+1}, \quad (2.12)$$

with

$$\frac{\partial u_i}{\partial x_i}^{n+1} = 0. \quad (2.13)$$

Here the superscript represents the time step, and the hat represents the intermediate step of the fractional-step method. In (2.11), a Crank–Nicolson scheme is used for the convective terms (in time derivatives) and the viscous terms that contain only the derivatives with respect to ζ. A second-order Adams–Bashforth scheme is used for the convective terms and the viscous terms that contain the derivatives with respect to ξ and ψ. The term C_i is expressed as

$$C_i = \rho\left(-\frac{\partial(u_i u)}{\partial \xi} - \frac{H_x' - \zeta H_x'}{H' + \overline{H}}\frac{\partial(u_i u)}{\partial \zeta} - \frac{\partial(u_i v)}{\partial \psi} - \frac{H_y' - \zeta H_y'}{H' + \overline{H}}\frac{\partial(u_i v)}{\partial \zeta} - \frac{1}{H' + \overline{H}}\frac{\partial(u_i w)}{\partial \zeta}\right) + \mu\nabla_{\xi\psi}^2 u_i. \quad (2.14)$$

Here the operators $\nabla_{\xi\psi}^2$ and ∇_ζ^2 are given in (2.9) and (2.10), respectively. With this decomposition for the viscous terms, the nonlinear equation (2.11) for the velocity at the intermediate step, $\hat{u}_i$, can be solved directly without iteration. On the other hand, the semi-implicit scheme is still used for the dominant vertical derivatives in the viscous terms, which is necessary to fully resolve the turbulent boundary layer with small grid size in the vertical direction and a relatively large time step. With the above-mentioned features, this modified fractional-step method is found to be computationally efficient in our simulation.

The scalar $\boldsymbol{\phi}$ in (2.12), called the pseudo-pressure, is related to the pressure by the equation

$$p^{n+1/2} = \boldsymbol{\phi}^{n+1} + \frac{\mu\Delta t}{2}\nabla^2\boldsymbol{\phi}^{n+1} \quad (2.15)$$

Boundary type	ak	c/u_*	$Re = U\lambda/\nu$
Stationary wavy wall	0.1	0	9491
	0.25	0	8181
Vertical waving wall	0.1	2 14 25	9208 9689 9943
	0.25	2 14 25	8454 9632 11 036
Airy wave	0.01	2	9535
	0.025	2	9687
	0.05	2	9772
	0.1	2 14 25	9208 9566 9953
	0.15	2	8922
	0.2	2	8445
	0.25	2 14 25	8501 9576 10 518
Stokes wave	0.25	2 14 25	8058 9755 11 008

TABLE 1. Parameters for wavy boundary conditions.

and is obtained by solving the Poisson equation

$$\frac{\partial}{\partial x_i}\left(\frac{\partial \boldsymbol{\phi}}{\partial x_i}^{n+1}\right) = -\frac{\rho}{\Delta t}\frac{\partial \hat{u}_i}{\partial x_i}, \tag{2.16}$$

which is obtained by applying the divergence operator to (2.12) and then substituting (2.13) into it. It is noted that after the algebraic mapping, the Laplacian operators in (2.16) become nonlinear. With the pseudo-spectral method in the horizontal directions, these equations need to be solved iteratively. The nonlinear form of (2.16) is rewritten as

$$\begin{aligned}
&\frac{\partial^2 \boldsymbol{\phi}}{\partial \xi^2}^{m+1} + \frac{\partial^2 \boldsymbol{\phi}}{\partial \psi^2}^{m+1} + \frac{1}{\overline{H}^2}\frac{\partial^2 \boldsymbol{\phi}}{\partial \zeta^2}^{m+1} \\
&\quad = \frac{\rho}{\Delta t}\frac{\partial \hat{u}_i}{\partial x_i} + \frac{1}{\overline{H}^2}\frac{\partial^2 \boldsymbol{\phi}}{\partial \zeta^2}^{m} - \frac{1+(H'_x-\zeta H'_x)^2+(H'_y-\zeta H'_y)^2}{(H'+\overline{H})^2}\frac{\partial^2 \boldsymbol{\phi}}{\partial \zeta^2}^{m} - 2\frac{H'_x-\zeta H'_x}{H'+\overline{H}}\frac{\partial^2 \boldsymbol{\phi}}{\partial \xi \partial \zeta}^{m} \\
&\qquad - 2\frac{H'_y-\zeta H'_y}{H'+\overline{H}}\frac{\partial^2 \boldsymbol{\phi}}{\partial \psi \partial \zeta}^{m} - \left(\frac{(H'_{xx}+H'_{yy})(1-\zeta)}{H'+\overline{H}} - 2\frac{(H'^2_x+H'^2_y)(1-\zeta)}{(H'+\overline{H})^2}\right)\frac{\partial \boldsymbol{\phi}}{\partial \zeta}^{m}.
\end{aligned} \tag{2.17}$$

Here the superscripts m and $m+1$ represent the previous and current iteration steps, respectively. A modified Newton's method is used to accelerate the convergence of the iteration (Shen *et al.* 2003). We found that for the simulations presented in the current paper, the residual error $|\boldsymbol{\phi}^{m+1} - \boldsymbol{\phi}^m|$ is reduced to less than 10^{-10} within six iterations (typically two to four iterations are sufficient in our simulation).

2.4. *Simulation parameters and boundary conditions*

In our simulation, the Reynolds numbers based on the wavelength λ and the mean velocity U at the top boundary, $Re \equiv U\lambda/\nu$, with $\nu = \mu/\rho$, are given in table 1. The computational domain size in the present work is 4λ (streamwise) $\times$ 3λ (spanwise) $\times$ 2λ (vertical). Periodic boundary conditions are used in the streamwise and spanwise directions. By checking the two point correlation, we have confirmed that the domain size is sufficiently large. With the resolution $(Nx, Ny, Nz) = (128, 128, 129)$, we have uniform grid sizes in the two horizontal directions, $\Delta\xi^+ = 8.84$ and $\Delta\psi^+ = 6.63$, and vertical grid sizes $\Delta\zeta^+ = 0.42$ near the top and bottom boundaries and $\Delta\zeta^+ = 8.45$ in

the middle of the channel. Here and hereafter, the superscript '+' denotes the velocity and length values normalized by wall variables u_* and ν/u_*, respectively. (On the basis of u_* and λ, the Reynolds number is $Re_* = u_*\lambda/\nu \approx 283$, which is about 10–40 % higher than the previous DNS studies by Sullivan *et al.* 2000, Kihara *et al.* 2007 and Lin *et al.* 2008, because of the increase in computer power; the grid resolutions are comparable.)

We consider four types of wavy boundary conditions in the present study: stationary wavy walls, vertically waving walls, Airy waves and Stokes waves. They are prescribed as the Dirichlet conditions at the wave surface (denoted by the subscript 's') for the turbulent flow according to the following formulations.

(i) Stationary wavy wall:

$$H' = -\eta_s = -a\sin kx, \tag{2.18}$$

$$(u_s, v_s, w_s) = (0, 0, 0). \tag{2.19}$$

(ii) Vertically waving wall:

$$H' = -\eta_s = -a\sin k(x - ct), \tag{2.20}$$

$$(u_s, v_s, w_s) = (0, 0, -akc\,\cos k(x - ct)). \tag{2.21}$$

(iii) Airy wave:

$$H' = -\eta_s = -a\sin k(x - ct), \tag{2.22}$$

$$(u_s, v_s, w_s) = (akc\,\sin k(x - ct), 0, -akc\,\cos k(x - ct)). \tag{2.23}$$

(iv) Stokes wave: the exact Stokes solution (Schwartz 1974) is used as a fully nonlinear water wave boundary condition. Following Dommermuth & Yue (1987), we directly solve the nonlinear equations associated with the mapping function in Schwartz (1974, (2.6)) by using Newton iteration.

Between Airy and Stokes waves, although the difference caused by the nonlinearity appears to be of secondary importance compared with the waveform itself (i.e. $O(ak)^2$ versus $O(ak)$; for $ak = 0.25$, the maximum relative difference is 12.1 %, 21.2 % and 7.2 % for surface elevation, streamwise velocity and vertical velocity, respectively), for some of the turbulence statistics, the difference is found to be appreciable. This wave nonlinearity effect is discussed in the later sections of the present paper.

In addition to the theoretical water wave boundary conditions in (iii) and (iv) above, we also consider the effect of wind-induced surface drift. Following Phillips & Banner (1974), the distribution of wind drift velocity q along the wave surface is written as

$$q = c - u_s - \sqrt{(c - u_s)^2 - q_0(2c - q_0)}. \tag{2.24}$$

Here c is the wave phase speed; u_s is the streamwise surface orbital velocity of the wave (by Airy or Stokes wave solutions); and q_0 is the mean wind-induced surface drift velocity (its value can be obtained by measurement). In the current paper, we choose $q_0 = 0.55u_*$ by compiling several existing experimental results (see e.g. Wu 1973; Phillips & Banner 1974). Equation (2.24) provides a surface drift current in the wind blowing direction with the maximum at the wave crest and the minimum at the wave trough.

In the present study, we consider two different wave steepnesses, namely $ak = 0.1$ and 0.25. The effect of wave phase speed is quantified by the wave age c/u_*, defined as the ratio between the wave phase speed c and the turbulence friction velocity u_*. The inverse wave age, u_*/c, indicates the level of wind forcing: for a given phase speed,

c/u_*	q_0/u_*	q_0/c	$q_0/c(2-q_0/c)$
2	0.55	0.275	0.474
14	0.55	0.039	0.077
25	0.55	0.022	0.044

TABLE 2. Estimation of the right-hand side of inequality (2.25).

larger u_*/c indicates stronger wind forcing. In the present study, we choose three different wave ages, namely $c/u_* = 2$, 14 and 25. Following Belcher & Hunt (1998), we use the wave age $c/u_* = 2$ to represent slow (young) waves, $c/u_* = 14$ for intermediate waves and $c/u_* = 25$ for fast (mature) waves. A list of wave boundary parameters is given in table 1. Note that the Airy wave is the linearized water wave solution and requires small wave steepness. In the current study, in addition to $ak = 0.1$, we also consider $ak = 0.25$ for the Airy wave case in order to make direct comparison with the cases of a stationary wavy wall and a vertically waving wall. In order to represent the nonlinear water wave with $ak = 0.25$, the Stokes wave solution has been used as we mentioned earlier. For an Airy wave with $c/u_* = 2$, five additional values of wave steepness, $ak = 0.01$, 0.025, 0.05, 0.15 and 0.2, are also considered to study the steepness effect on wind–wave interaction.

When the wind-induced surface drift effect is considered, one important question is whether wave breaking happens or not. As given by Banner & Phillips (1974), with the surface drift, the criterion that wave breaking does not happen can be described as

$$(1-ak)^2 > \frac{q_0}{c}\left(2-\frac{q_0}{c}\right). \tag{2.25}$$

The left-hand side of (2.25) has the values of 0.81 and 0.5625 for $ak = 0.1$ and 0.25, respectively. The right-hand side of (2.25) is listed in table 2. As shown, for all the water wave cases considered in the current paper, the values of $(1-ak)^2$ are larger than the values of $(2-q_0/c)\,q_0/c$. This ensures that the wind-induced surface drift effect we considered here does not cause wave breaking.

2.5. *Definition of statistical quantities*

In our DNS, we start the simulation with a three-dimensional velocity field prescribed as the summation of a two-dimensional mean flow and three-dimensional random perturbations as seeds for the turbulence. The turbulent Couette flow is then developed dynamically because of flow instability. After the turbulence has fully developed, we start to study flow statistics. In the DNS, no turbulence model is used (cf. (2.1)), and the exact velocity components (u, v, w) and pressure are obtained as functions of (x, y, z, t). For turbulence statistics, in order to study the interaction of turbulence with surface waves, the phase-average approach (Hussain & Reynolds 1970) is used to quantify the modulation of statistical properties of turbulence by the underlying wave motion. Since the reference frame in our simulation is fixed in space and the surface wave propagates in the x-direction with a phase speed c, we define the phase average of a function $f(x(i), y(j), z(k), t(n))$ as

$$\langle f\rangle^0(x,z) \equiv \frac{1}{Nt \times Ny}\sum_{n=1}^{Nt}\sum_{j=1}^{Ny} f(x(i)+c\,t(n), y(j), z(k), t(n)), \tag{2.26}$$

where the indices i, j, k, n are for discrete grid points in x, y, z and t, respectively, and Ny and Nt are the total numbers of sample points in y and t, respectively. With this approach, the function f is averaged over the spanwise direction and also over its period in time. This phase average is then further averaged over all the waves in the streamwise direction of the computational domain:

$$\langle f\rangle(x,z) \equiv \frac{1}{Nw}\sum_{m=0}^{Nw-1}\langle f\rangle^0(x+m\lambda,z). \tag{2.27}$$

Here Nw is the number of waves in the domain along the streamwise direction ($Nw=4$ in our case) and λ is the wavelength. The fluctuation is then defined as $f'(x,y,z,t)=f(x,y,z,t)-\langle f\rangle(x-ct,z)$. The phase-averaged quantity can be further decomposed into $\langle f\rangle(x,z)=[f](z)+f_w(x,z)$, where $[f]$ and f_w are the plane average and wave-induced variation of f, respectively.

By applying the above-given analysis, we decompose the instantaneous three-dimensional turbulence flow field $\boldsymbol{u}(x,y,z,t)$ into

$$\boldsymbol{u}(x,y,z,t)=\langle\boldsymbol{u}\rangle(x,z)+\boldsymbol{u}'(x,y,z,t)=[\boldsymbol{u}](z)+\boldsymbol{u}_w(x,z)+\boldsymbol{u}'(x,y,z,t). \tag{2.28}$$

The velocity fluctuation $\boldsymbol{u}'$ is then used in the following sections to calculate turbulence quantities such as Reynolds stress and TKE.

With the above-given definition of phase average, only one wavelength in the streamwise direction is necessary when statistics of turbulence are plotted. However, for a better visualization of the turbulence structures, we plot two wavelengths instead in most of the figures of the present paper.

In the present study, all the computations were carried out for about 13 500 viscous time units (tu_*^2/ν). Statistics are obtained from 160 instantaneous flow field data points with an approximate time interval of 27 viscous time units.

To confirm that the sample number for statistics in the current paper is sufficient for convergence, we repeat the calculation of statistical quantities with different sampling spaces. It is found that reducing the sample number to 80 results in a very small difference in the statistics compared with the values obtained with 160 samples. For example, for all the cases, the change in the momentum flux is less than 4 %, and the change in the wave form drag is less than 3 %. We also repeat the calculation by increasing the sample number to 320. The comparison with the results using 160 samples shows less than 1 % differences in the statistical quantities. The above-given validation indicates that the sample number of 160 used in the analysis is adequate for the statistical quantities reported in the present paper.

3. Mean flow structure

3.1. *Mean streamline pattern*

Figure 3 shows the phase-averaged streamline pattern of $(\langle u\rangle - c, \langle w\rangle)$ over various wavy boundaries with steepness $ak=0.25$. In the frame travelling with wave, far from the surface the mean flow is in the direction of wave propagation, while near the wave surface the mean flow reverses and is in the direction opposite to wave propagation. Therefore, there exists a critical layer where the mean velocity $\langle u\rangle$ matches the wave phase speed c, i.e. $\langle u\rangle - c=0$. The critical layer is plotted as the dash-dot-dotted lines in figure 3. The critical layer is surrounded by closed streamlines, known as the cat's eyes (Lighthill 1962).

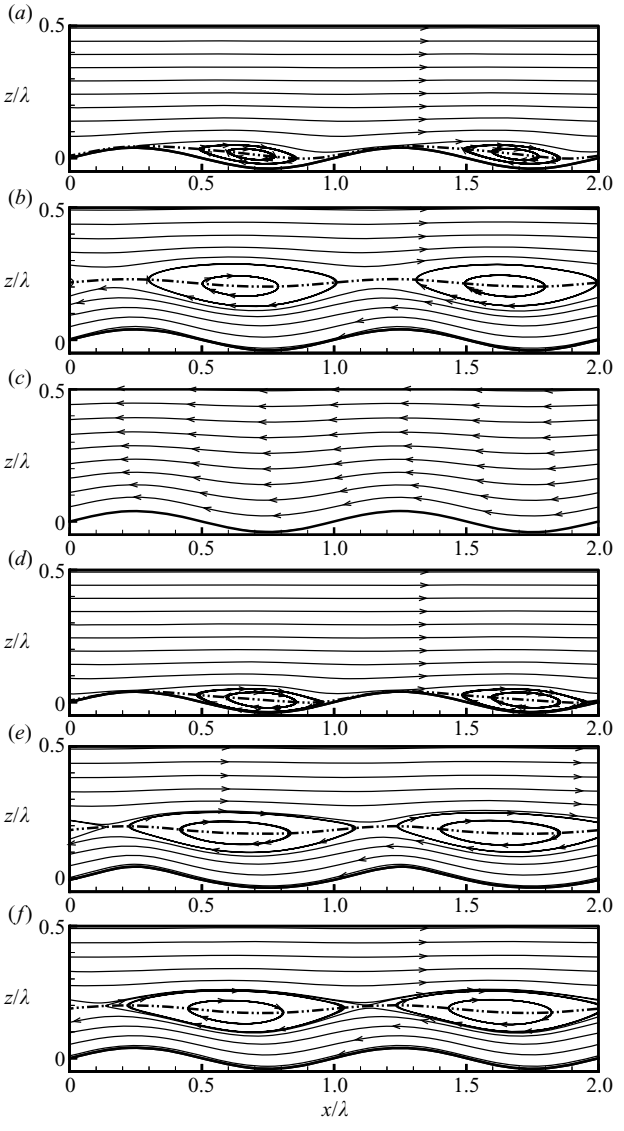

FIGURE 3. Phase-averaged streamline pattern over various wavy boundaries with steepness $ak = 0.25$, including the following: Airy waves with wave ages (*a*) $c/u_* = 2$, (*b*) $c/u_* = 14$ and (*c*) $c/u_* = 25$; (*d*) Airy wave with surface drift and $c/u_* = 2$; (*e*) Stokes wave with $c/u_* = 14$; and (*f*) vertically waving wall with $c/u_* = 14$. The velocity used for calculating streamlines is in the wave-following frame, i.e. $(\langle u \rangle - c, \langle w \rangle)$ is used in the plots. The dash-dot-dotted lines represent the critical layer where $\langle u \rangle - c = 0$.

Figure 3(*a–c*) shows the phase-averaged streamline pattern over Airy waves with various wave ages. As we can see, for the case of $c/u_* = 2$, the critical layer lies very close to the wave surface; for the case of $c/u_* = 14$, the critical layer lies some distance above the wave surface, and the mean flow reverses below the critical layer; for the case of $c/u_* = 25$, the critical layer is located far away from the wave surface and is beyond the domain plotted (but still within the computational domain), resulting in negligible dynamic effect on the wave. Figure 3(*d*) shows the streamline pattern

over Airy waves of $c/u_* = 2$ with the wind-induced surface drift present. Comparison between figures 3(a) and 3(d) shows that for the slow-wave case, the centre of the cat's eyes shifts downstream from $(x, z)/\lambda = (0.689, 0.015)$ to $(x, z)/\lambda = (0.741, 0.008)$ because of the surface drift. The influence of surface drift on the streamline pattern is small for the intermediate- and fast-wave cases, which are not shown here because of space limitation.

Figure 3(e) shows the streamline pattern for the case of Stokes waves with $c/u_* = 14$. By comparing with figure 3(b), we find that at $x/\lambda = 0.5$ the Stokes wave case has a critical height of about $z/\lambda = 0.018$ that is smaller than the value of $z/\lambda = 0.021$ for the Airy wave case. Note that a Stokes wave has larger streamwise velocity at the crest and smaller streamwise velocity at the trough compared with the Airy wave with the same $(ak, c/u_*)$. Therefore, in the frame travelling with the wave, the turbulence over a Stokes wave has smaller reversed mean flow near the wave surface compared with the Airy wave case. This results in a lower height of the critical layer for the Stokes wave case. For the wave age of $c/u_* = 2$, the nonlinearity effect is not obvious, since the magnitude of the wave orbital velocity is small. For the wave age of $c/u_* = 25$, the nonlinearity effect on the streamline pattern is also small. Because the critical layer is located beyond the domain we plotted, the Stokes wave case has a similar parallel streamline pattern as the Airy wave case except that the streamline curvatures are slightly larger near the crest and slightly smaller near the trough. Because of space limitation, the cases of $c/u_* = 2$ and 25 are not shown in the present paper.

The streamline pattern over the vertically waving wall is found to be similar to the Airy wave case, except for the case of $c/u_* = 14$ (see figure 3f) in that the critical layer has about the same height as in the Stokes wave case, while it is lower than that in the Airy wave case.

The streamline patterns over moving boundaries with steepness $ak = 0.1$ are similar to those with $ak = 0.25$ but have lower critical layers and smaller vertical extension of the cat's eyes, due to the smaller wave surface orbital velocities. Because of space limitation, these streamline patterns are not shown in the present paper.

3.2. *Mean velocity*

Flow separation over a wavy boundary is an important phenomenon. For turbulence over a stationary wavy boundary, boundary layer separation happens on the lee of the crest for large wave steepness. Figure 4(a, b) shows the phase-averaged streamwise velocity $\langle u \rangle$ in turbulence over stationary wavy surfaces with $ak = 0.1$ and 0.25, respectively. For the case of $ak = 0.1$, $\langle u \rangle$ is positive everywhere, and thus there is no mean flow separation. For the case of $ak = 0.25$, there exists a reverse-flow region above the wave trough, indicating the occurrence of mean flow separation (because $\langle u \rangle = 0$ at the stationary wavy wall). The mean flow separates around $x = 0.47\lambda$ and reattaches around $x = 0.88\lambda$ (wave crest is at $x = 0.25\lambda$ and trough is at $x = 0.75\lambda$). Figure 4(c) shows the contours of $\langle u \rangle$ for a vertically waving boundary with $(ak, c/u_*) = (0.25, 2)$. Since in the frame fixed in space $\langle u \rangle$ is zero everywhere on the surface, the small region of negative $\langle u \rangle$ indicates the occurrence of mean flow separation. The mean flow separates at around $x = 0.65\lambda$ and reattaches at $x = 0.81\lambda$.

For the turbulence over a moving wave surface, the mean flow separation is more likely to happen for small c/u_* (corresponding to strong wind forcing) compared with large c/u_*. Therefore, here we focus on moving wave surface cases with $c/u_* = 2$. Figure 4(d, e) shows $\langle u \rangle$ contours over Airy waves and Stokes waves with $(ak, c/u_*) = (0.25, 2)$. Because of the negative surface orbital velocity above the wave trough, the negative $\langle u \rangle$ region there cannot be regarded as the sign of flow separation.

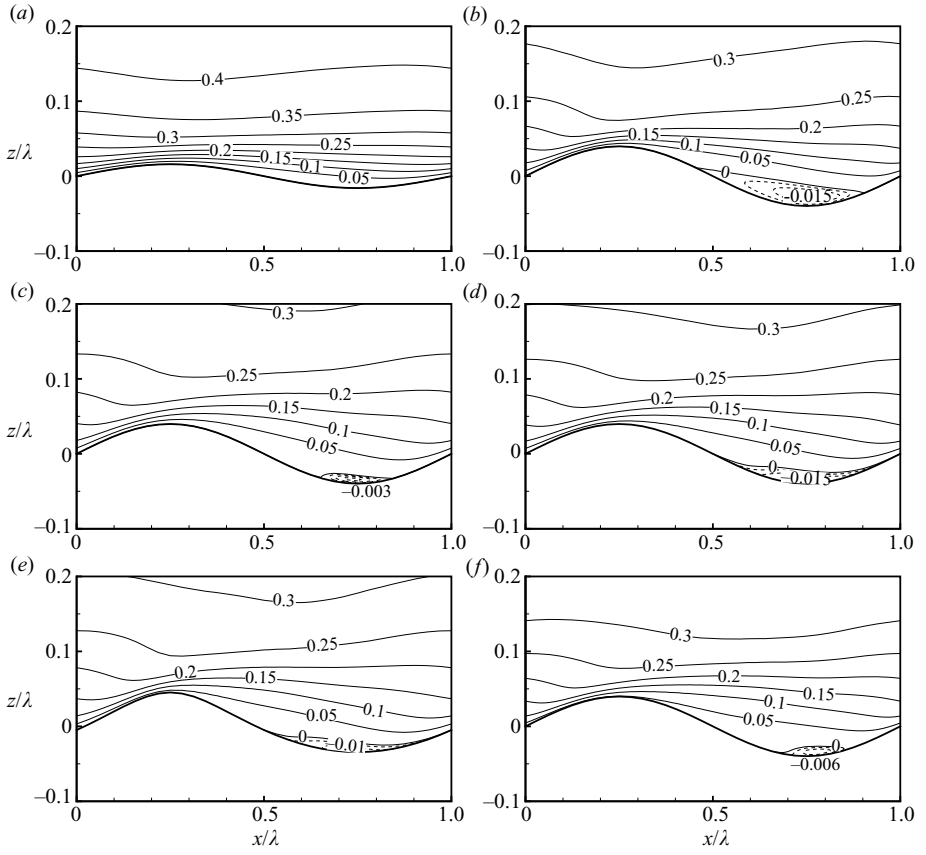

FIGURE 4. The phase-averaged streamwise velocity contours over different wavy boundaries. (*a*) Stationary wavy wall with $ak = 0.1$; (*b*) stationary wavy wall with $ak = 0.25$; (*c*) vertically waving wall with $(ak, c/u_*) = (0.25, 2)$; (*d*) Airy wave with $(ak, c/u_*) = (0.25, 2)$; (*e*) Stokes wave with $(ak, c/u_*) = (0.25, 2)$; and (*f*) Airy wave with surface drift and with $(ak, c/u_*) = (0.25, 2)$. The dashed contour lines represent negative values. In (*c*)–(*f*), the surface waves propagate in the $+x$-direction.

Figure 4(*f*) shows the Airy wave case of $(ak, c/u_*) = (0.25, 2)$ with the wind-induced surface drift. With the surface drift in the x-direction, the size of the negative $\langle u \rangle$ region is reduced.

Precise detection and detailed measurement in laboratory and field of air flow separation over the wave surface is challenging. Banner & Melville (1976) showed the occurrence of air flow separation over a breaking wave (which produces a stagnation point) on the leeward side of the crest. Banner (1990) and Babanin *et al.* (2007) measured the effect of wave breaking on air pressure distribution and showed the influence on wave growth rate. Donelan *et al.* (2006) showed separation over a slow steep wave at the crest (this full separation has the reattachment well up the windward side of the preceding wave crest), which is caused by insufficient centripetal acceleration from pressure gradients. By using a digital particle image velocimetry technique, Reul, Branger & Giovanangeli (1999) and Veron *et al.* (2007) were able to elucidate the separation flow pattern and shear stress variation over breaking waves. Reul *et al.* (2008) measured the detailed structure of air flow separation over breaking water waves with various wind forcing levels and wave breaking intensities.

Their measurement captured the streamline pattern of the separation bubble over micro-breaking, gentle-spilling breaking, spilling breaking and plunging breaking waves. They also showed unsteady patch-like vorticity, which exists both in the shear layer at the edge of the separation bubble and in the region near the reattachment point.

Effect of flow separation on the wind–wave interaction dynamics is clearly shown in the numerical simulation by Maat & Makin (1992) and in the WOWC theory prediction by Makin & Kudryavtsev (2002). In the present work, wave breaking is not represented by the prescribed surface wave motion; nor is the wave crest sharp enough. Therefore, we do not expect to capture these large-scale separations in our simulation. This is shown in the mean streamline pattern plotted in figure 3. As pointed out by Gent & Taylor (1977), the occurrence of separation requires the streamlines intersecting with the wave surface. In figure 3, we do not see evidence for the occurrence of mean flow separation for the water wave cases considered in the current paper.

4. Instantaneous flow field

4.1. *Instantaneous flow separation*

Although no obvious mean flow separation is found for $c/u_* = 2$ in our DNS results, there may still exist instantaneous flow separations that occur intermittently both in space and in time. To check this, we first calculate the surface shear stress to narrow down the search region for instantaneous separation. The surface shear stress is given as

$$\tau_s = \boldsymbol{t_x} \boldsymbol{\Sigma} \boldsymbol{n}^{\boldsymbol{T}}. \tag{4.1}$$

Here the normal and tangential direction vectors of the wave surface are

$$\left.\begin{aligned} \boldsymbol{n} &= \frac{\{H_x', 0, 1\}}{\sqrt{H_x'^2 + 1}}, \\ \boldsymbol{t_x} &= \frac{\{1, 0, -H_x'\}}{\sqrt{H_x'^2 + 1}}, \end{aligned}\right\} \tag{4.2}$$

respectively, and the stress tensor is

$$\Sigma_{ij} = -p\delta_{ij} + \mu\left(\frac{\partial u_i}{\partial x_j} + \frac{\partial u_j}{\partial x_i}\right). \tag{4.3}$$

Figure 5 shows the contours of instantaneous surface shear stress above the Stokes wave with $(ak, c/u_*) = (0.25, 2)$. The dashed contour lines indicate negative surface shear stress. It is found that upwind of the wave troughs, large negative surface shear stress occurs intermittently. For a Stokes wave with $ak = 0.25$, the negative surface shear stress region occupies about 18.2 % of the total surface area.

As pointed out by Gent & Taylor (1977), a negative shear stress on a moving surface does not necessarily indicate flow separation. Separation occurs when the streamline leaves the surface. The large negative surface shear stress region shown in figure 5 suggests possible locations for such events. From our instantaneous three-dimensional DNS data, we examine the velocity field in detail. The results can be well represented

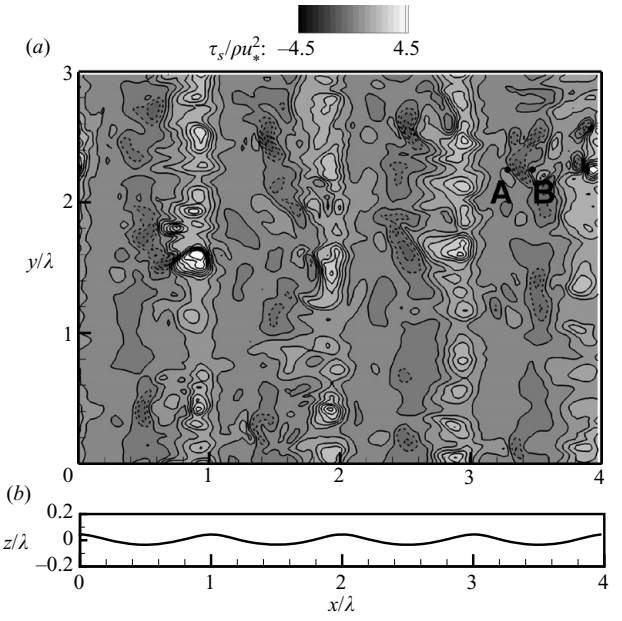

FIGURE 5. (*a*) The contours of the instantaneous surface stress on a Stokes wave with $ak = 0.25$ and $c/u_* = 2$. The dashed contour lines represent negative values. (*b*) Instantaneous surface wave elevation. The surface wave propagates in the $+x$-direction.

by the velocity of the turbulence relative to the surface wave motion:

$$\left.\begin{aligned} u_r(x, y, z, t) &= u(x, y, z, t) - u_s(x, y, t), \\ w_r(x, y, z, t) &= w(x, y, z, t) - w_s(x, y, t). \end{aligned}\right\} \tag{4.4}$$

Here (u, w) are the velocity components for the instantaneous turbulence field and (u_s, w_s) are the velocities of surface wave motion. Note that the turbulent velocities at (x, y, z) are subtracted by the wave motion at the same horizontal position (x, y). Therefore, in the near-wall region, the vector (u_r, w_r) indicates the relative motion of turbulent fluid to the surface particles of the water wave. Figure 6 shows the vectors of relative velocities (u_r, w_r) in the (x, z)-plane with $y/\lambda = 2.25$ at the same instantaneous time as in figure 5. The vertical length is rescaled for better visualization. Here the surface points A and B indicate the same locations as in figure 5. We found that the fluid from upstream and downstream converges around point A, and the velocity vectors point away from the surface above point A. This indicates the occurrence of instantaneous flow separation from the wave surface around point A. Around point B, the fluid upstream and downstream diverges, and the velocity vectors point towards the surface. This indicates the reattachment of the separated flow. We note that when the intermittent flow separation occurs, the local variation of instantaneous streamline and shear stress is quite pronounced. We calculated the positive and negative values of the instantaneous surface shear stress over the entire wave surface, which are denoted as τ_s^+ and τ_s^-, respectively. For their maximum values, we found that the ratio $|\tau_s^-|_{max}/|\tau_s^+|_{max}$ is $O(1)$. This is in contrast with the ratio of the phase-averaged values, which was found to be two orders of magnitude smaller in our study (results not plotted here).

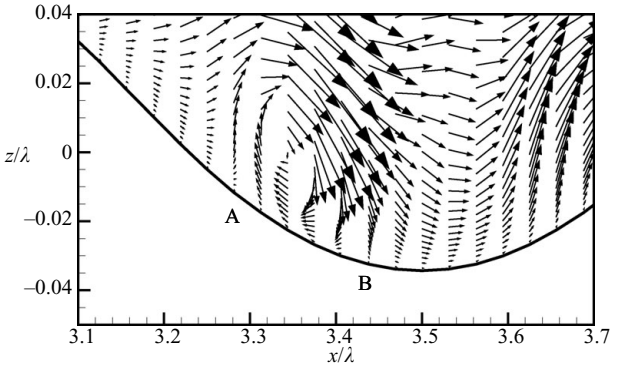

FIGURE 6. Vectors of instantaneous relative velocity $(u_r, w_r) = (u(x, z) - u_s(x), w(x, z) - w_s(x))$ in the (x, z)-plane of $y/\lambda = 2.25$ of figure 5. Here (u, w) are the instantaneous streamwise and vertical velocities of turbulence and (u_s, w_s) are the surface velocity of the wave. The points A and B correspond to the points A and B in figure 5(*a*), respectively. The surface wave propagates in the $+x$-direction.

As mentioned earlier, Donelan *et al.* (2006) showed the occurrence of flow separation over slow steep waves. It should be pointed out that their measurements were performed at Lake George in Australia. Being constrained by the depth of the lake, the water waves in their measurements belong to the transitional water depth condition. Therefore, the nonlinearity of the surface wave in their measurements is stronger than that of the deep-water waves in the present study.

As a consequence of the weaker wave nonlinearity in the present simulation, the intermittent separation shown here corresponds to conditions milder than the ones discussed in Donelan *et al.* (2006) and Babanin *et al.* (2007). The size and intensity of the instantaneous separation shown in figures 5 and 6 is not as marked as the full separation shown in Donelan *et al.* (2006). Donelan *et al.* (2006) showed that for their slow-wave case LG8 that has $U_{10}/c = 7.2$, full separation happens over waves of $ak > 0.25$, which are about 28 % of all the waves in their record.

The significance of the full separation phenomenon has been clearly revealed by Donelan *et al.* (2006) with their wave-follower pressure data. They showed that when full separation happens, the air pressure variation becomes smaller than the corresponding non-separation case; meanwhile, the phase shift of the pressure field relative to the waveform increases. These two effects work in the opposite way in affecting the pressure-induced wave form drag. Their combined effect may result in positive or negative influence on the wind–wave momentum transfer. The condition of full separation goes beyond the capability of the current DNS approach, which uses a prescribed waveform that is still relatively mild (e.g. not sharp and asymmetric enough at the wave crest). To study the air flow separation over surface waves with more realistic waveforms, we are currently extending our turbulence simulation capability by two approaches. In the first approach, the air turbulence simulation is coupled with a water turbulence simulation with both tangential and normal stresses balanced on the deformable wave interface. In the second approach, the air turbulence simulation is coupled with a water wave simulation by a high-order spectral method (Dommermuth & Yue 1987). For both of these two coupled simulations, the water wave evolves dynamically under the influence of air turbulence. These provide us with the capability of studying the air flow separation over a more realistic wind wave surface. However, this goes beyond the scope of the current work. Much more

work needs to be done in this area for us to have a better understanding of the flow separation over surface waves, and the results will be reported in the future.

4.2. *Instantaneous vortical structures*

Previous studies of the turbulence boundary layer of a flat wall have indicated the existence and the dynamic importance of coherent vortical structures (e.g. Kim 1983; Moin & Kim 1985; Robinson 1991; Adrian, Meinhart & Tomkins 2000). On the basis of experimental and numerical observations, many conceptual models for near-wall coherent turbulent structures have been proposed, among which the quasi-streamwise vortex model (e.g. Jeong *et al.* 1997) and the horseshoe vortex model (e.g. Zhou *et al.* 1999) are the most widely studied. For turbulence over wavy surfaces, however, there is a lack of studies on coherent vortical structures. The few existing studies are all for stationary wavy walls (e.g. De Angelis *et al.* 1997; Calhoun & Street 2001; Nakagawa, Na & Hanratty 2003; Tseng & Ferziger 2004).

For the study of coherent vortical structures in turbulence, many identification methods have been developed for the visualization of vortices (see the review by Chakraborty, Balachandar & Adrian 2005). Without losing generality, we use the λ_2 method (Jeong & Hussain 1995) for vortex identification in the current paper. We calculate the eigenvalues of the tensor $\boldsymbol{S}^2 + \boldsymbol{\Omega}^2$, where $\boldsymbol{S}$ and $\boldsymbol{\Omega}$ are respectively the symmetric and antisymmetric parts of the velocity gradient tensor $\nabla \boldsymbol{u}$. Let λ_2 be the second largest eigenvalue, the region in which $\lambda_2 < 0$ defines the interior of a vortex core.

In figure 7 we plot the instantaneous coherent vortical structures in the near-surface region for slow ($c/u_* = 2$), intermediate ($c/u_* = 14$) and fast ($c/u_* = 25$) Airy waves with steepness $ak = 0.25$. The vortical structures are represented by the isosurface of $\lambda_2 = -1$. It is apparent that the dominant vortical structures near the wave surface are stretched in the streamwise direction for all cases. By comparing figures 7(a) and 7(c), we note that features of the coherent vortices strongly depend on the wave age c/u_*.

In the case of $c/u_* = 2$ (figure 7a), the coherent vortical structures lie above the wave surface. Most of the vortices are along the streamwise direction, while some others have the shape of a horseshoe with a spanwise component. We characterize the vortical structures by two categories. The first is quasi-streamwise vortices, e.g. vortices 1–3 in figure 7(a). We found that the quasi-streamwise vortical structures start from the windward side of a wave crest and then extend over the crest. The second type of vortical structure is the horseshoe vortices, e.g. vortices 4–6. It is interesting that these horseshoe vortices have their heads upstream and legs downstream. This is the opposite of the typical horseshoe vortices near a flat wall, of which the heads are downstream of the legs (see e.g. Adrian 2007). We found that the heads of these vortices are usually located above the wave trough.

In the case of $c/u_* = 14$ (figure 7b), the coherent vortical structures are almost all aligned in the streamwise direction. The spatial frequency of the vortices is less than that in the $c/u_* = 2$ case. The largest vortex has the streamwise dimension of about λ, longer than that in the case of $c/u_* = 2$. In addition to these isolated vortical structures, underneath them there are long spanwise vortex sheets lying right above the wave crests and troughs. Our study shows that these vortex sheets have vorticity vectors pointing in the spanwise direction. The spanwise vorticity ω_y is negative above the crest and positive above the trough. This sign distribution suggests that the spanwise vortex sheet is generated by the strong periodic surface wave motion.

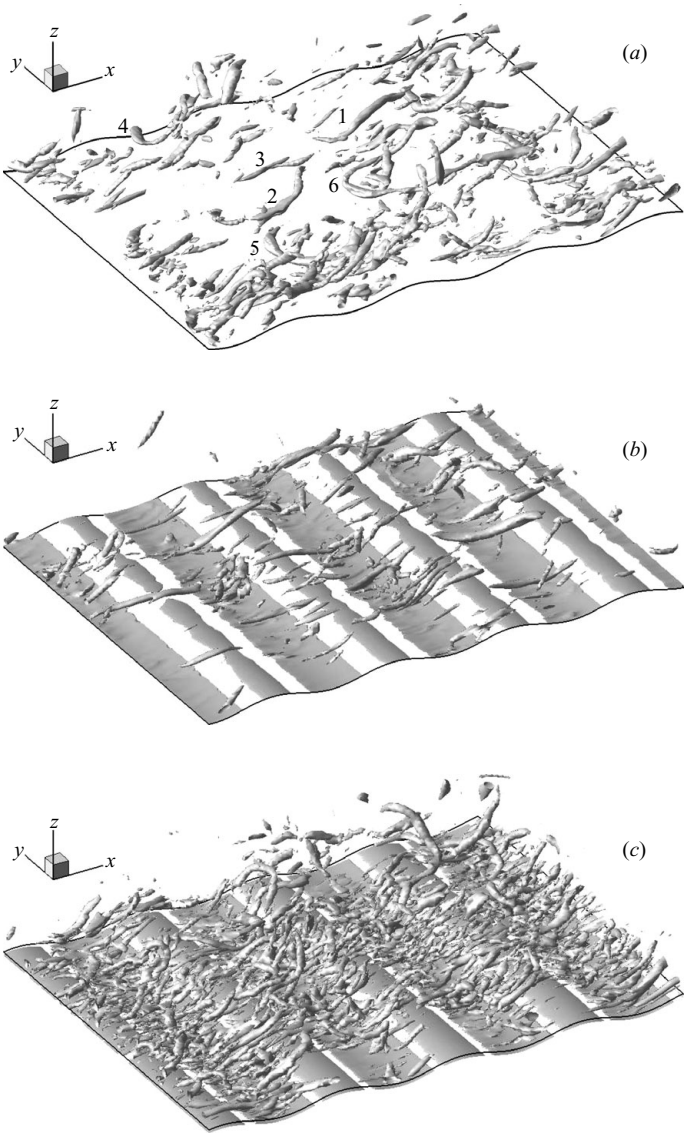

FIGURE 7. Snapshot of near-surface coherent vortical structures in instantaneous turbulence field over Airy waves with steepness $ak = 0.25$ and wave ages (*a*) $c/u_* = 2$, (*b*) $c/u_* = 14$ and (*c*) $c/u_* = 25$. The vortical structures are represented by the isosurface of $\lambda_2 = -1$. For the slow-wave case, two kinds of typical vortical structures are identified: quasi-streamwise vortices, e.g. vortices 1–3; horseshoe vortices, e.g. vortices 4–6. For the intermediate- and fast-wave cases, the characteristic vortical structures are bent quasi-streamwise vortices. The surface wave propagates in the $+x$-direction.

In the case of $c/u_* = 25$ (figure 7*c*), the spanwise vortex sheets become wider in the streamwise direction than those in the $c/u_* = 14$ case, because of the stronger surface wave motion with the larger c value. The coherent vortices are still mainly along the streamwise direction. The spatial frequency of the vortices is higher than those in the cases of $c/u_* = 2$ and $c/u_* = 14$. Meanwhile, the size of vortices is reduced, with the largest streamwise dimension about $\lambda/2$.

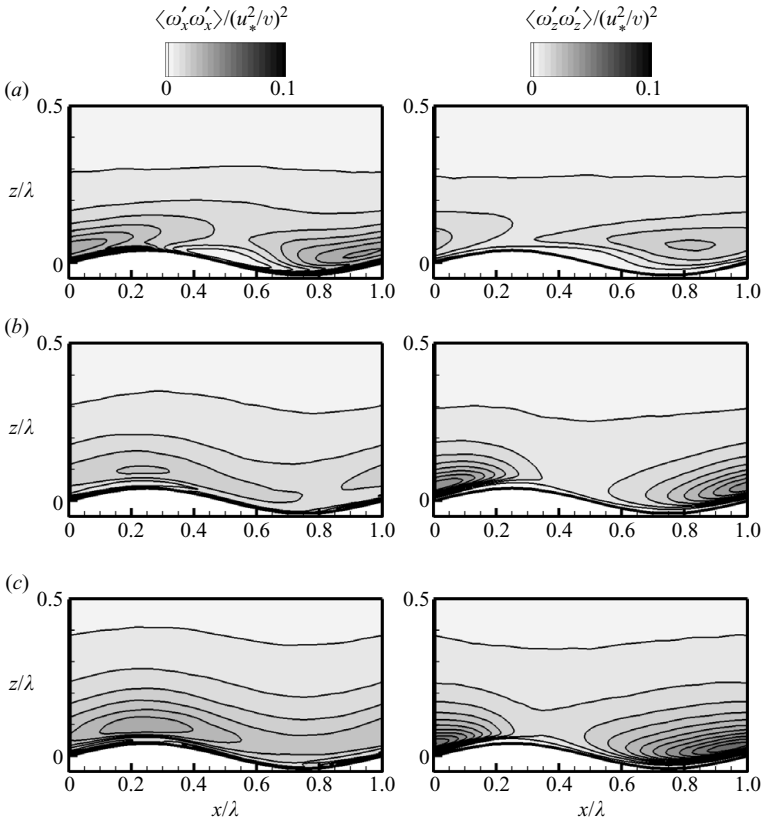

FIGURE 8. The contours of $\langle\omega_x'\omega_x'\rangle$ and $\langle\omega_z'\omega_z'\rangle$ normalized by $(u_*^2/\nu)^2$ for Airy wave case with $ak = 0.25$: (*a*) $c/u_* = 2$, (*b*) $c/u_* = 14$, (*c*) $c/u_* = 25$. The surface wave propagates in the $+x$-direction.

The characteristics of the instantaneous vortical structures discussed above are consistent with the statistics of the vorticity fluctuations. Figure 8 shows the streamwise and vertical components of the phase-averaged enstrophy $\langle\omega_i'\omega_i'\rangle$. For the slow-wave case, the high-intensity region of $\langle\omega_x'\omega_x'\rangle$ is located on the windward side of the wave. The high-intensity region of $\langle\omega_z'\omega_z'\rangle$ is located above the wave trough, with a smaller peak than that of $\langle\omega_x'\omega_x'\rangle$. A comparison between the statistical result in figure 8(*a*) and the direct observation in figure 7(*a*) indicates that for the slow-wave case, the quasi-streamwise vortices on the windward side have vorticity vectors parallel to the wave surface and therefore have a larger component in the x-direction than in the z-direction. These quasi-streamwise vortices start from the trough, extend to the downstream direction, lift up above the crest and then become weak above the lee side of the crest. This variation is found to be similar to the distribution of Reynolds stress due to $Q2$ events, which will be discussed in § 5.3.

When the wave age increases to $c/u_* = 14$ and 25, the high-intensity region of $\langle\omega_x'\omega_x'\rangle$ is located above the wave crest, while the high-intensity region of $\langle\omega_z'\omega_z'\rangle$ is located above the windward side. The location difference between $\langle\omega_x'\omega_x'\rangle_{max}$ and $\langle\omega_z'\omega_z'\rangle_{max}$ implies the change of primary direction of the vortices over the wave crest. Direct observation of the instantaneous vortical structures in figure 7(*b*, *c*) confirms this change of vortex direction: the quasi-streamwise vortices are along the streamwise

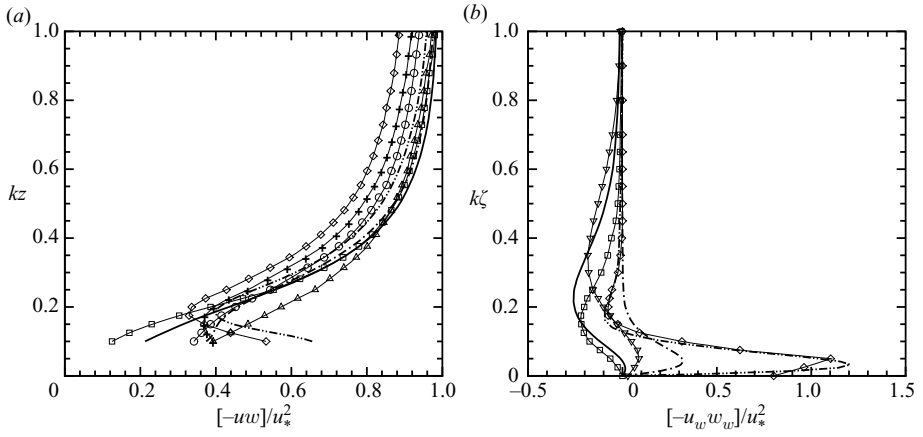

FIGURE 9. Comparison of the vertical profiles of the averaged (a) total momentum flux $[-uw]/u_*^2$ and (b) wave-induced momentum flux $[-u_w w_w]/u_*^2$ for Airy waves with $ak = 0.1$ and various wave ages. Values of current DNS results are denoted by the thick lines: ——, $c/u_* = 2$; — ·—, $c/u_* = 14$; — ··—, $c/u_* = 25$. DNS results of Sullivan *et al.* (2000) are denoted by the thin lines with symbols: —□—, $c/u_* = 0$; —▽—, $c/u_* = 3.9$; —△—, $c/u_* = 7.84$; —○—, $c/u_* = 11.5$; —+—, $c/u_* = 16.2$; —◇—, $c/u_* = 22.7$.

direction above the wave crest and bend downward to the vertical direction above the windward side of the crest (when observed in the wave following frame, the near-surface vortices propagate in the $-x$-direction for the cases of $c/u_* = 14$ and 25). Meanwhile, the spatial frequency of the vortices above the windward side (bending downward to the vertical direction) is larger than those above the wave crest (primarily pointing in the streamwise direction), especially for the case of $c/u_* = 25$ (figure 7c). The higher frequency of vortices above the windward side is consistent with the result in figure 8(b,c), which shows that the peak value of $\langle \omega_z' \omega_z' \rangle$ is higher than the peak value of $\langle \omega_x' \omega_x' \rangle$.

The results given above indicate strong and complex dependence of near-surface coherent vortical structures on the surface wave motion. A more detailed and extended study on the dynamics of the near-surface coherent vortical structures, which goes beyond the scope of the current paper, is reported in Yang & Shen (2009).

5. Wave effect on turbulence statistics

5.1. *Vertical profiles of averaged momentum flux*

In this section, we show the vertical profiles of the plane-averaged momentum flux. With the values of u and w obtained from DNS and based on the variable decomposition defined in (2.28), the plane-averaged total momentum flux $[-uw]$ can be decomposed as

$$[-uw] = -[u][w] + [-u_w w_w] + [-u'w'] \,. \tag{5.1}$$

Figure 9 shows the vertical profile of the total momentum flux $[-uw]$ and the wave-induced flux $[-u_w w_w]$ for the water wave cases with $ak = 0.1$. The DNS results from Sullivan *et al.* (2000) are also plotted for comparison. The effect of a surface wave on the momentum flux is mainly in the near-surface region and is more clearly indicated by $[-u_w w_w]$ in figure 9(b). When the wave age is small, $[-u_w w_w]$ is negative near the wave surface; as the wave age increases, $[-u_w w_w]$ increases and becomes more

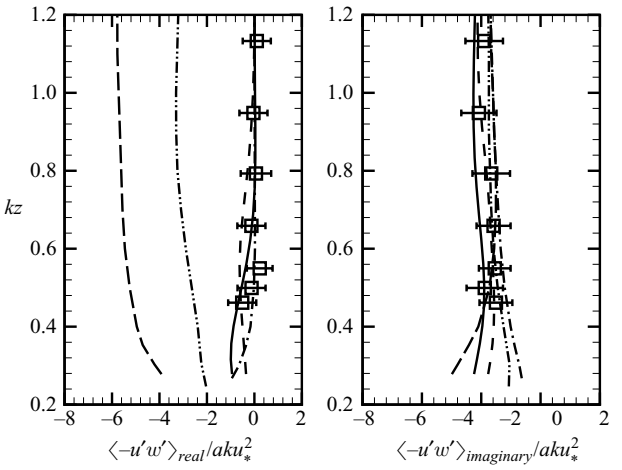

FIGURE 10. The profiles of the real and imaginary parts of Reynolds stress normalized by aku_*^2. Values of current DNS results: ——, Airy wave with $(ak, c/u_*) = (0.1, 2)$; – – –, Airy wave with $(ak, c/u_*) = (0.25, 2)$. Measurement results of Mastenbroek (1996; also see Mastenbroek *et al.* 1996) with $(ak, c/u_*) = (0.18, 4.3)$ are denoted by □ with an error bar. Model results of Mastenbroek (1996) with different turbulence closures are also plotted: — —, mixing length; — ·· —, e-ϵ; — · —, LRR.

positive. Our DNS result shows a trend of momentum flux variation consistent with Sullivan *et al.* (2000).

We then compare the distribution of Reynolds stress $\langle -u'w' \rangle$ with the experiment and model results of Mastenbroek *et al.* (1996). Following Mastenbroek *et al.* (1996), in figure 10 we present the Reynolds stress distribution in terms of the components in and out of phase with the wave, which are termed the real and imaginary parts of Reynolds stress, respectively. The comparison indicates that our DNS result agrees well with their measurements and supports the LRR closure model.

5.2. *Wave effect on Reynolds stress*

We next investigate the (x, z)-distribution of Reynolds stress, which is highly dependent on the wave condition and is important to many processes including turbulence transport and production. Figure 11 shows the contours of the normalized Reynolds stress $\langle -u'w' \rangle / u_*^2$ in flows over an Airy wave with $ak = 0.25$ and $c/u_* = 2$, 14 and 25. It is apparent that the Reynolds stress distribution is strongly dependent on wave phase, and this dependence changes drastically with wave age. For the case of $(ak, c/u_*) = (0.25, 2)$, the distribution of Reynolds stress is asymmetric about the wave crest. The maximum Reynolds stress lies above the wave trough at $(x, z - \eta(x))/\lambda = (0.812, 0.099)$ with the peak value about 1.67. Besides this apparent peak region, there exists a second high-Reynolds-stress region that extends from the first to the upward downstream direction over the wave crest. All together, the positive-Reynolds-stress region rides above the windward side of the wave crest and is almost parallel to the slope of the windward surface. Meanwhile, there is a small region with negative Reynolds stress very close to the wave surface on the windward side of the crest with the peak value -0.33 at $(x, z - \eta(x))/\lambda = (1.092, 0.013)$. For $(ak, c/u_*) = (0.25, 14)$, as the wave age increases, the size of the negative-Reynolds-stress region increases, and the peak value also increases to about -1.30 around the position $(x, z - \eta(x))/\lambda = (1.0, 0.029)$. Meanwhile, the positive peak of Reynolds stress

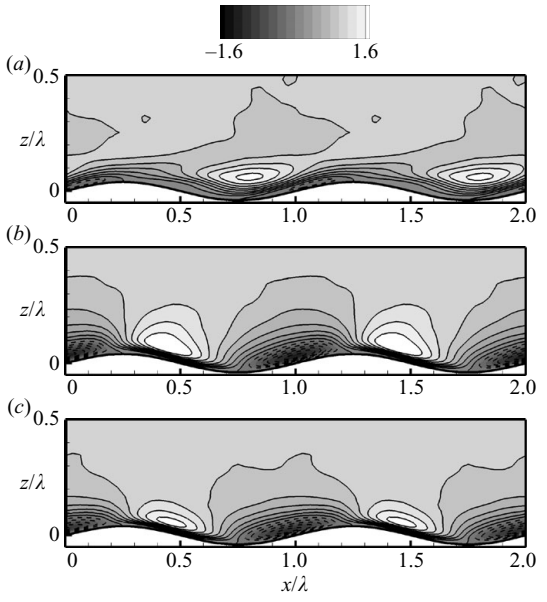

FIGURE 11. The contours of normalized Reynolds stress $\langle -u'w' \rangle / u_*^2$ over Airy wave with steepness $ak = 0.25$ and wave ages (*a*) $c/u_* = 2$, (*b*) $c/u_* = 14$ and (*c*) $c/u_* = 25$. The surface wave propagates in the $+x$-direction. The dashed contour lines represent negative values. The contour interval is 0.2.

shifts upstream to $(x, z - \eta(x))/\lambda = (0.438, 0.056)$, and its value increases to about 1.86. The positive and negative contours of Reynolds stress become more symmetric about the wave crest compared with the case of $c/u_* = 2$. As the wave age further increases to $c/u_* = 25$, both positive and negative peaks of Reynolds stress become slightly weaker than in the case of $c/u_* = 14$. The positive peak value reduces to 1.71, and its location moves slightly upstream to $(x, z - \eta(x))/\lambda = (0.469, 0.043)$. The negative peak reduces to -1.10, and its location also moves slightly upstream to $(x, z - \eta(x))/\lambda = (0.969, 0.028)$.

The distribution of Reynolds stress shown above is consistent with the result of Kihara *et al.* (2007). In their paper, they calculated the wave-induced Reynolds stress over Airy waves with steepness $ak = 0.1$ and wave ages $c/u_* \in (0, 20)$. The wave-induced Reynolds stress, $(-u'w')_w$, is defined as

$$(-u'w')_w = \langle -u'w' \rangle - [-u'w']. \tag{5.2}$$

In the present study, we find that $\langle -u'w' \rangle$ is better, since it is more directly related to the near-surface turbulent motions. The correlation between $\langle -u'w' \rangle$ and the near-surface coherent vortical structures is discussed later in §§ 5.3 and 7.

The cases of Stokes waves, Airy waves with surface drift and a vertically waving wall have similar spatial distributions of Reynolds stress as the Airy wave case. Because of space limitation, their contours are not shown here. In order to make a quantitative comparison, we plot the profiles of Reynolds stress along a constant height above the wave surface with $ak = 0.25$ and $c/u_* = 2$, 14 and 25 for all these cases in figure 12. The heights above the wave surface are chosen as $(z - \eta)/\lambda = 0.1$ ($\approx$28 wall units) for $c/u_* = 2$ and $(z - \eta)/\lambda = 0.05$ ($\approx$14 wall units) for $c/u_* = 14$ and 25. Here the heights are chosen to be close to the peaks of Reynolds stress as shown in figure 11.

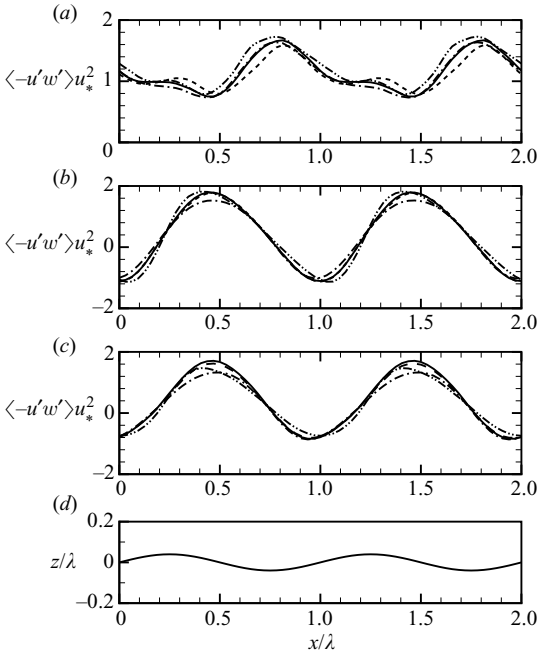

FIGURE 12. Profiles of normalized Reynolds stress $\langle -u'w' \rangle / u_*^2$ above wavy surfaces with steepness $ak = 0.25$ and wave ages (*a*) $c/u_* = 2$, (*b*) $c/u_* = 14$ and (*c*) $c/u_* = 25$: ——, Airy wave; — ·· —, Stokes wave; – – –, Airy wave with surface drift; — · —, vertically waving wall. For $c/u_* = 2$, the profiles are at the height $(z - \eta)/\lambda = 0.1$; for $c/u_* = 14$ and 25, the profiles are at the height $(z - \eta)/\lambda = 0.05$. The surface wave elevation for the Airy wave case is plotted in (*d*) to indicate the wave phase. The surface wave propagates in the $+x$-direction.

For the case of $c/u_* = 2$ (figure 12*a*), the profiles of Reynolds stress depart from the sinusoidal shape and are asymmetric about the wave crest. The Stokes wave case has higher Reynolds stress everywhere along the wave profile than the Airy wave case, and the high-Reynolds-stress region shifts towards the upstream direction compared with the Airy wave case. In contrast with the effect of surface nonlinearity, the existence of surface drift results in a reduction of Reynolds stress and a phase shift of the high-Reynolds-stress region towards the downstream direction. The vertically waving wall case has similar Reynolds stress profile as the Airy wave case, except for the slightly smaller value above the wave crest.

For the case of $c/u_* = 14$ (figure 12*b*), the Reynolds stress profiles become closer to the sinusoidal shape and more symmetric about the wave crest compared with the case of $(ak, c/u_*) = (0.25, 2)$. Compared with the Airy wave case, the profile for the Stokes wave case has almost the same peak values. However, the streamwise distance between the locations of the positive and negative peaks decreases from 0.455 for the Airy wave case to 0.373 for the Stokes wave case. The vertically waving wall case has a similar profile as the Airy wave case but with smaller positive and negative peaks on the lee and windward sides, respectively.

The profiles for the case of $c/u_* = 25$ (figure 12*c*) are similar to those for $c/u_* = 14$ but with smaller peak values. Unlike for $c/u_* = 2$, for $c/u_* = 25$ the Stokes wave case has smaller peak values than the Airy wave case. The waving wall case has a similar profile as the Airy wave case but with a smaller positive peak on the lee side. For

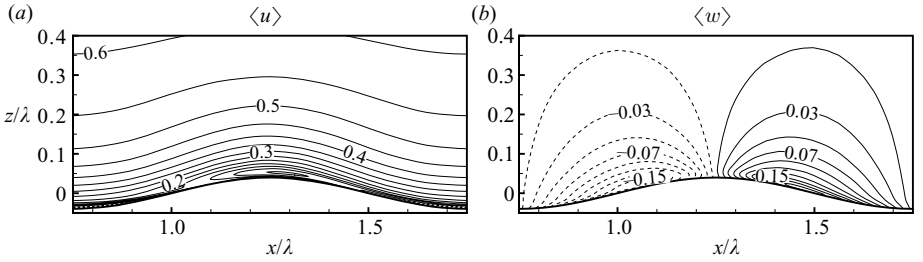

FIGURE 13. The phase-averaged velocity contours for the Airy wave case with $(ak, c/u_*) = (0.25, 25)$: (a) streamwise velocity component, (b) vertical velocity component. The dashed contour lines represent negative values. The surface wave propagates in the $+x$-direction.

both $c/u_* = 14$ and 25, the effect of surface drift on Reynolds stress distribution is small because of the small ratio of q_0/c as listed in table 2.

The distributions of Reynolds stress over water waves with $ak = 0.1$ are similar to those for $ak = 0.25$ but with smaller peak values and therefore weaker streamwise variation. Because of space limitation, the Reynolds stress distribution for the case of $ak = 0.1$ is not shown in the current paper.

As pointed out by Hudson (1993), for turbulence over a stationary wavy wall, there exists a thin region with small negative Reynolds stress on the windward side of the crest. Hudson (1993) attributed this negative Reynolds stress to an artefact of the Cartesian coordinate system used in their simulation and analysis. However, earlier laboratory experiments (see the review of Ursell 1956) on solid and water waves showed quite different air flow structures between the two types of problems, which led to the theoretical developments by Phillips (1957) and Miles (1957) and many subsequent studies. The argument of Hudson (1993) may be inadequate to explain the existence of the negative-Reynolds-stress region with large magnitude and large size as shown in figure 11(b,c). When the water wave moves fast, the magnitude of the vertical velocity in the turbulence induced by the wave motion is comparable to the mean streamwise velocity. Similar to the negative correlation between u' and w' in a boundary layer flow with a mean shear $U(z)$, the wave-induced vertical velocity here creates a shear flow $W(x)$ in the vertical direction. The contours of phase-averaged streamwise and vertical velocities in the case of an Airy wave with $(ak, c/u_*) = (0.25, 25)$ are shown in figure 13. A streamwise fluctuation u' with the shear profile $W(x)$ on the windward side results in a positive correlation of u' and w', i.e. a negative Reynolds stress. In this case, the sweep and ejection on the windward side are respectively not indicated by $w' < 0$ and $w' > 0$ but by $u' < 0$ and $u' > 0$ instead. This will be further discussed in §§ 5.3 and 7.

In summary, as the wave age increases, Reynolds stress $\langle -u'w' \rangle$ near the wave surface transits from an asymmetric distribution with a positive peak above the wave trough to a more symmetric distribution with a negative peak on the windward side and a positive peak on the lee side of the wave. This indicates the transition of the wave boundary effect on turbulence from the geometric feature dominant for the slow-wave case to the kinematic feature dominant for the fast-wave case. The wave nonlinearity effect also indicates this transition. The surface-drift-induced reduction and phase shift of Reynolds stress is only appreciable for the slow-wave case and can be interpreted as a consequence of the fact that the surface drift releases part of the

shear stress when it drifts with the mean turbulence flow towards the downstream direction.

5.3. *Quadrant analysis*

A useful tool in the study of Reynolds stress is quadrant analysis. The contribution to Reynolds stress is divided into four quadrants: $Q1$ ($u'>0$, $w'>0$), $Q2$ ($u'<0$, $w'>0$), $Q3$ ($u'<0$, $w'<0$) and $Q4$ ($u'>0$, $w'<0$). Previous research shows that $Q2$ and $Q4$ motions dominate in the turbulence boundary layer of a flat wall, which are associated with ejection and sweep events, respectively (Kim, Moin & Moser 1987). However, as shown in § 5.2, for waves with relatively large phase speed, $Q2$ and $Q4$ do not necessarily indicate ejections and sweeps. The classification of ejection and sweep depends on local profiles of u and w.

Sullivan *et al.* (2000) calculated the quadrants of $(\langle u\rangle, \langle w\rangle)$ in a horizontal plane near the wave surface. They showed a difference between turbulence over water waves and that over a flat wall. In the present study, we further apply the quadrant analysis to the turbulent momentum flux $u'w'$ at four different wave phases and at two different heights above the wave surface.

Figure 14(i) shows the quadrants of (u', w') above the Airy wave of $(ak, c/u_*) = (0.25, 2)$. The vertical height above wave surface in terms of the wall units is $(z-\eta)^+ = 5.3$. Four different streamwise locations are chosen: (a) windward side of crest $(x/\lambda = 0)$, (b) crest $(x/\lambda = 0.25)$, (c) leeward side of crest $(x/\lambda = 0.5)$ and (d) trough $(x/\lambda = 0.75)$. It is found that at this low height, above the windward side and wave crest the turbulent events cover all quadrants, while above the leeward side and trough, $Q2$ and $Q4$ dominate. On the leeward side, the amplitudes of u' and w' are much smaller than those at the other three locations. As shown in figure 14(ii), when the height increases to $(z-\eta)^+ = 17.8$, the situation becomes similar to the turbulence over a flat wall in that $Q2$ and $Q4$ events dominate at all of the streamwise locations. On the leeward side, however, the dominance of $Q2$ and $Q4$ seems weaker than at the other three locations.

Figure 15(i) shows the quadrants of (u', w') above an Airy wave with $(ak, c/u_*) = (0.25, 25)$ at $(z-\eta)^+ = 5.3$. Because of the much stronger wave motion than that in the slow-wave case, the distribution of (u', w') over the fast wave shows significant wave phase dependence and streamwise variation. For all of the four streamwise locations, the most significant contribution comes from the right half of the domain in which $u'>0$, and the amplitude of u' there is much larger than that in the left half of the domain. On the windward side of the wave crest, unlike the flat-wall case, the $Q1$ and $Q3$ events dominate. Above the crest and on the leeward side, $Q2$ and $Q4$ dominate instead. Above the trough, (u', w') has more equal contributions from the upper and lower halves of the domain than at the other three streamwise locations.

Figure 15(ii) shows the quadrants of (u', w') for $(ak, c/u_*) = (0.25, 25)$ when the height increases to $(z-\eta)^+ = 17.8$. It is found that the distributions at $(z-\eta)^+ = 17.8$ are similar to those at $(z-\eta)^+ = 5.3$, except for the larger amplitude of w' at the higher location. The comparison between figures 14(ii) and 15(ii) indicates that as the wave age increases, the influence of the surface wave motion on the quadrants extends further into the bulk flow.

The Reynolds stress can be decomposed into contributions from the four quadrants. Figure 16 shows the decomposed-Reynolds-stress distributions over an Airy wave with $(ak, c/u_*) = (0.25, 2)$. It is apparent that for this slow-wave case, the $Q2$ and $Q4$ events are responsible for most of the Reynolds stress, while the contributions from $Q1$ and

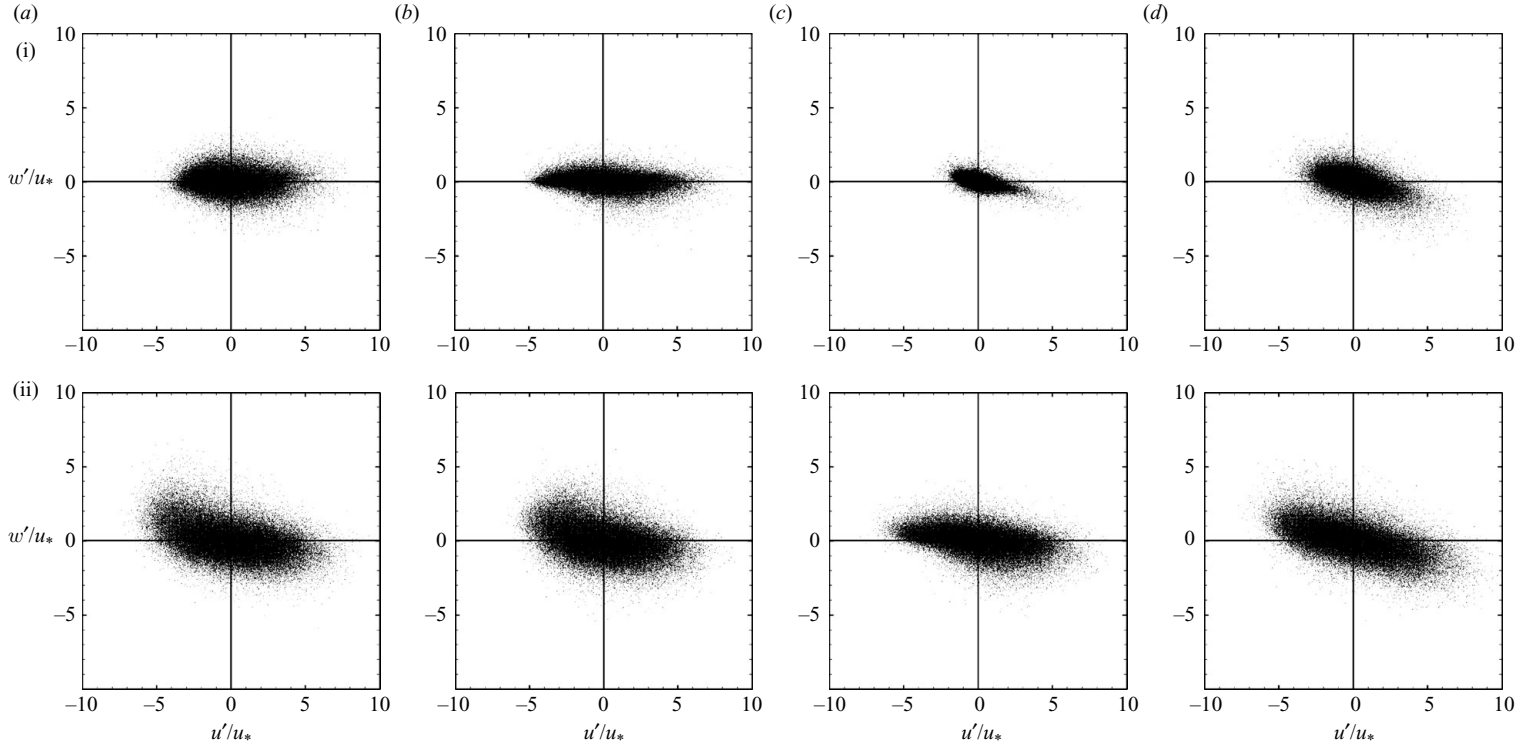

FIGURE 14. Distribution of $(u', w')/u_*$ at (i) $(z-\eta)^+ = 5.3$ and (ii) $(z-\eta)^+ = 17.8$ above slow water wave with $(ak, c/u_*) = (0.25, 2)$. Different streamwise locations are chosen: (*a*) above the windward side ($x/\lambda = 0.0$), (*b*) above the crest ($x/\lambda = 0.25$), (*c*) above the leeward side ($x/\lambda = 0.5$), (*d*) above the trough ($x/\lambda = 0.75$).

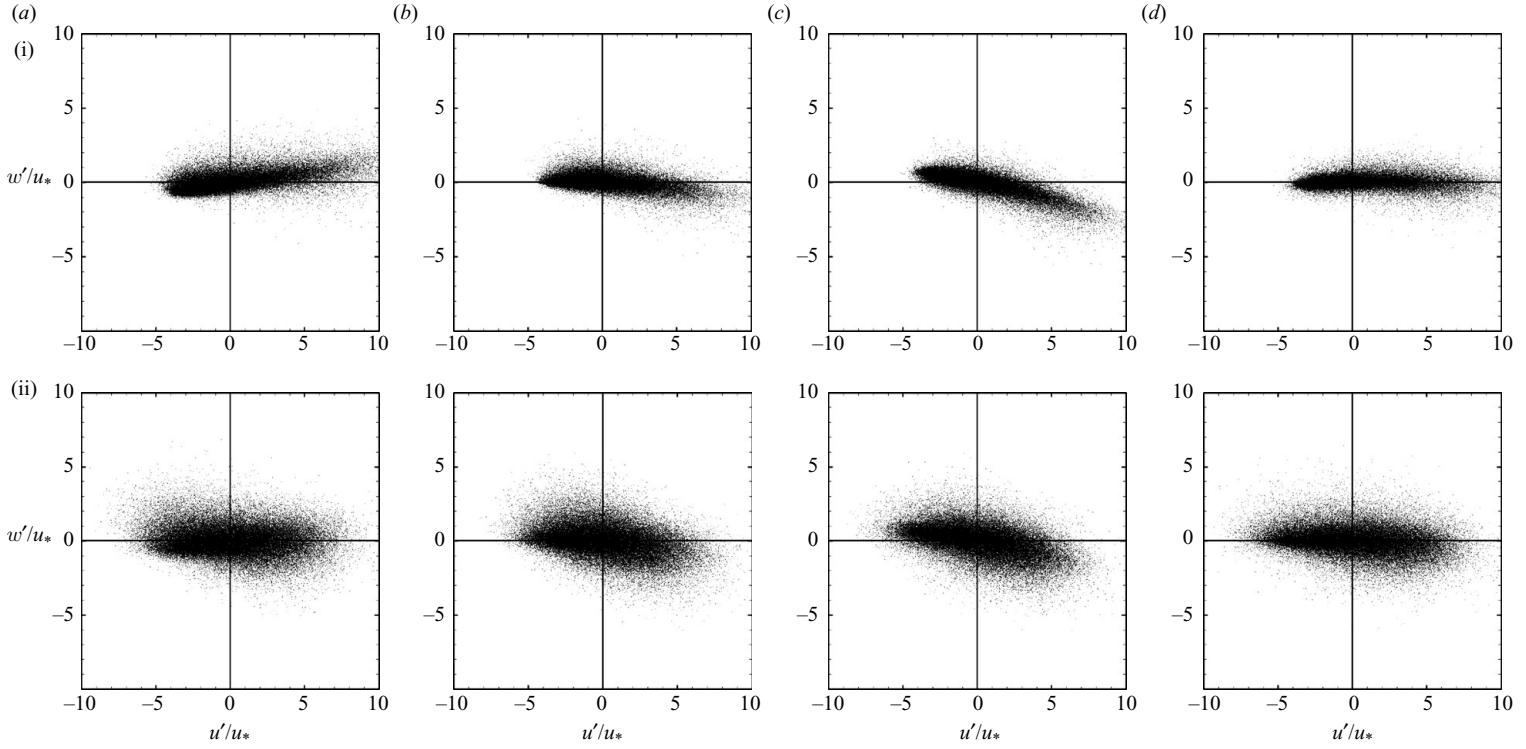

FIGURE 15. Distribution of $(u', w')/u_*$ at (i) $(z-\eta)^+ = 5.3$ and (ii) $(z-\eta)^+ = 17.8$ above fast water wave with $(ak, c/u_*) = (0.25, 25)$. Different streamwise locations are chosen: (*a*) above the windward side ($x/\lambda = 0.0$), (*b*) above the crest ($x/\lambda = 0.25$), (*c*) above the leeward side ($x/\lambda = 0.5$), (*d*) above the trough ($x/\lambda = 0.75$).

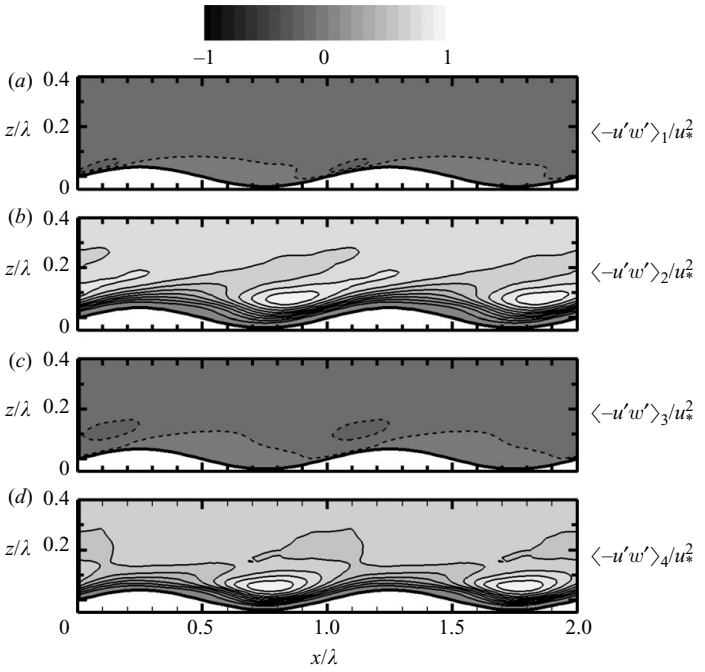

FIGURE 16. For the case of an Airy wave with $(ak, c/u_*) = (0.25, 2)$, contributions to Reynolds stress from quadrants: (a) $Q1$ $(u' > 0, w' > 0)$, (b) $Q2$ $(u' < 0, w' > 0)$, (c) $Q3$ $(u' < 0, w' < 0)$ and (d) $Q4$ $(u' > 0, w' < 0)$. The dashed contour lines represent negative values. The contour interval is 0.1. The surface wave propagates in the $+x$-direction.

$Q3$ are much smaller. In figure 16(b), the peak value of Reynolds stress due to $Q2$ (ejection in this case) starts above the wave trough, extends to the downstream direction, lifts up above the wave crest and then becomes weak further downstream. This distribution is found to be similar to the distribution of the quasi-streamwise vortices shown in figures 7(a) and 8(a). This similarity suggests that for the slow-wave case, ejection events on the windward side of the wave crest are correlated with the quasi-streamwise vortices. In figure 16(d), the peak value due to $Q4$ (sweep in this case) is located right above the wave trough. Therefore, we conclude that the primary peak region above the wave trough in figure 11(a) is generated by both the sweep and ejection events, while the secondary peak region above the windward side and crest is mainly due to the ejection event.

The distributions of the decomposed Reynolds stress over an Airy wave with $(ak, c/u_*) = (0.25, 25)$ are shown in figure 17. The distributions for $(ak, c/u_*) = (0.25, 14)$ are similar and are not shown here. It is found that for the fast-wave case, the $Q1$ and $Q3$ events produce negative Reynolds stress on the windward side of the wave crest, while $Q2$ and $Q4$ events contribute to positive Reynolds stress on the leeward side of the wave crest. For negative Reynolds stress, the contribution from $Q1$ is larger than that from $Q3$, while for positive Reynolds stress, $Q4$ makes more contribution than $Q2$. This is consistent with the result in figure 15(i), which shows that the events with $u' > 0$ have much larger amplitude than those with $u' < 0$.

Previous research has indicated that in a turbulent boundary layer flow, the distribution of the Reynolds stress $\langle -u'w' \rangle$ is related to the near-surface coherent turbulence motions and the vortical structures associated with these motions (see e.g.

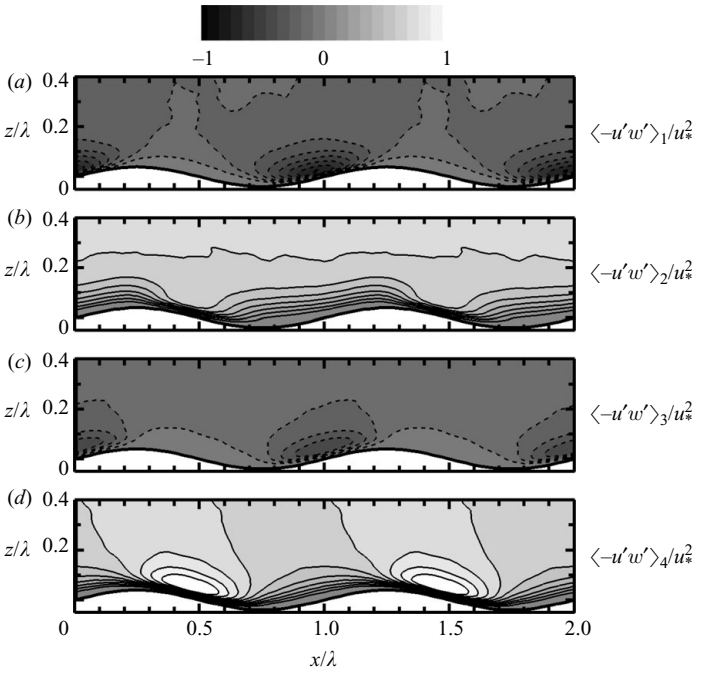

FIGURE 17. Same as in figure 16 but for $(ak, c/u_*) = (0.25, 25)$.

Robinson 1991). The decomposition of Reynolds stress shown above indicates clearly the correlation of Reynolds stress with near-surface turbulence motions. Further discussion of the relation between the Reynolds stress and the vortical structures is provided in § 7.

5.4. *Turbulent kinetic energy*

Figure 18 shows contours of turbulence intensities $\langle u'^2 \rangle$, $\langle v'^2 \rangle$ and $\langle w'^2 \rangle$ for turbulence over Airy waves with $ak = 0.25$ and $c/u_* = 2$, 14 and 25. It is found that in the near-surface region, the amplitudes of the three components of turbulence intensity have the order of $\langle u'^2 \rangle > \langle v'^2 \rangle > \langle w'^2 \rangle$.

For the slow wave $c/u_* = 2$, the high-intensity region of $\langle u'^2 \rangle$ coincides with the high-value region of Reynolds stress, which is located above the wave trough. This high-intensity region starts from the wave crest, extends to above the trough and reaches the peak value of 3.78 at $(x, z)/\lambda = (0.757, 0.084)$. It further extends over the next crest, with the band of this high-intensity region almost parallel to the windward side of the wave. The high-intensity region of $\langle v'^2 \rangle$ is located very close to the windward side of the wave crest, with a peak value of 1.77 at $(x, z)/\lambda = (1.011, 0.030)$. The high-intensity region of $\langle w'^2 \rangle$ is also located near the windward side but with a lower peak value of 0.63 at a higher location $(x, z)/\lambda = (0.861, 0.055)$ than that of $\langle v'^2 \rangle$.

For the intermediate wave $c/u_* = 14$, the high-intensity region of $\langle u'^2 \rangle$ is located on the windward side of the crest with a peak value of 4.81 at $(x, z)/\lambda = (1.023, 0.056)$, which coincides with the high-negative region of Reynolds stress. The peak of $\langle v'^2 \rangle$ with the value of 1.29 is also located above the windward side but at a higher height $(x, z)/\lambda = (0.930, 0.119)$ than the peak of $\langle u'^2 \rangle$. The intensity of $\langle w'^2 \rangle$ reduces

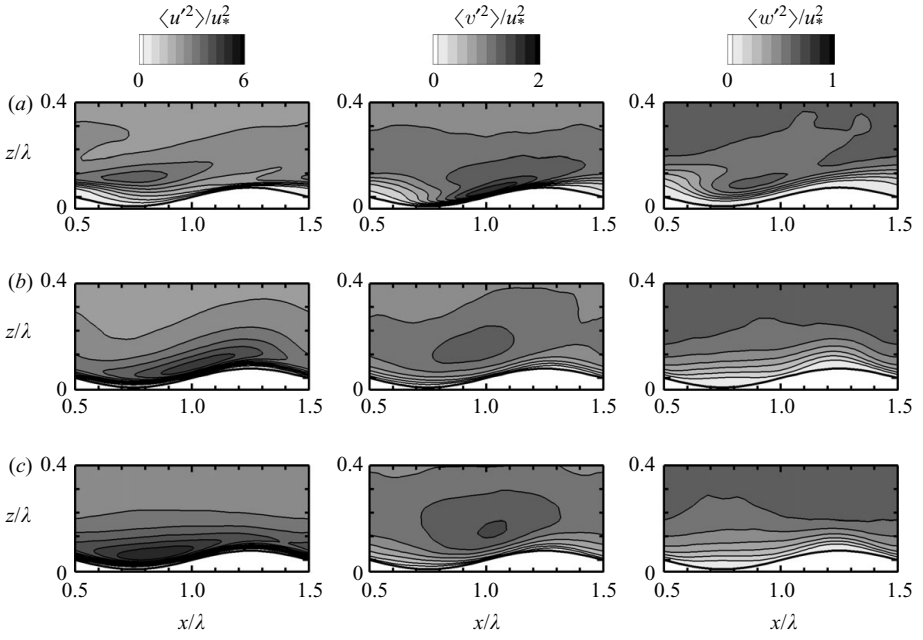

FIGURE 18. The contours of turbulence intensity (normalized by u_*^2) over Airy waves with steepness $ak = 0.25$ and wave ages (*a*) $c/u_* = 2$, (*b*) $c/u_* = 14$ and (*c*) $c/u_* = 25$. The surface wave propagates in the $+x$-direction.

monotonically when the wave surface is approached. Right above the wave crest and trough, there exist two regions with low $\langle w'^2\rangle$ intensity.

For the fast wave $c/u_* = 25$, the high-intensity region of $\langle u'^2\rangle$ is still located close to the windward side but with a higher peak value of 5.48 and is closer to the trough at $(x, z)/\lambda = (0.839, 0.023)$ compared with the $c/u_* = 14$ case. Similar to the $c/u_* = 14$ case, the high-intensity region of $\langle v'^2\rangle$ is located near the windward side at $(x, z)/\lambda = (1.031, 0.132)$ with a peak value of 1.43. The near-surface distribution of $\langle w'^2\rangle$ for $c/u_* = 25$ is similar to the $c/u_* = 25$ case.

The equation for the budgets of TKE (Hussain & Reynolds 1970) can be written as

$$\frac{\partial}{\partial t}\left(\frac{1}{2}\langle u_i' u_i'\rangle\right) = \underbrace{-\langle u_j\rangle \frac{\partial}{\partial x_j}\left(\frac{1}{2}\langle u_i' u_i'\rangle\right)}_{A} \underbrace{-\langle u_i' u_j'\rangle \frac{\partial \langle u_i\rangle}{\partial x_j}}_{P} \underbrace{-\frac{\partial}{\partial x_i}\left\langle \frac{p'}{\rho} u_i'\right\rangle}_{T_p} + \underbrace{\left\langle \frac{p'}{\rho}\frac{\partial u_i'}{\partial x_i}\right\rangle}_{\phi}$$
$$+ \underbrace{\nu \frac{\partial^2}{\partial x_j \partial x_j}\left(\frac{1}{2}\langle u_i' u_i'\rangle\right)}_{D_v} \underbrace{-\nu\left\langle \frac{\partial u_i'}{\partial x_j}\frac{\partial u_i'}{\partial x_j}\right\rangle}_{\epsilon} \underbrace{-\frac{\partial}{\partial x_j}\left(\frac{1}{2}\langle u_i' u_i' u_j'\rangle\right)}_{T_t}. \quad (5.3)$$

Here, A is the advection term; P is the production term; T_p is the pressure transport term; ϕ is the pressure–strain correlation term; D_v is the viscous diffusion term; ϵ is the dissipation term; and T_t is the turbulence transport term. When repeating index is applied to the subscript 'i', (5.3) represents the balance of the total TKE $(1/2)\langle u'^2 + v'^2 + w'^2\rangle$. When the subscript '$i$' is fixed, (5.3) with $i = 1$, 2 or 3 represents the balance of budgets for $(1/2)\langle u'^2\rangle$, $(1/2)\langle v'^2\rangle$ and $(1/2)\langle w'^2\rangle$, respectively.

Figure 19 shows the mean profiles of the budget terms of the total TKE for the turbulence over Airy waves with $ak = 0.25$ and $c/u_* = 2$, 14 and 25. Following

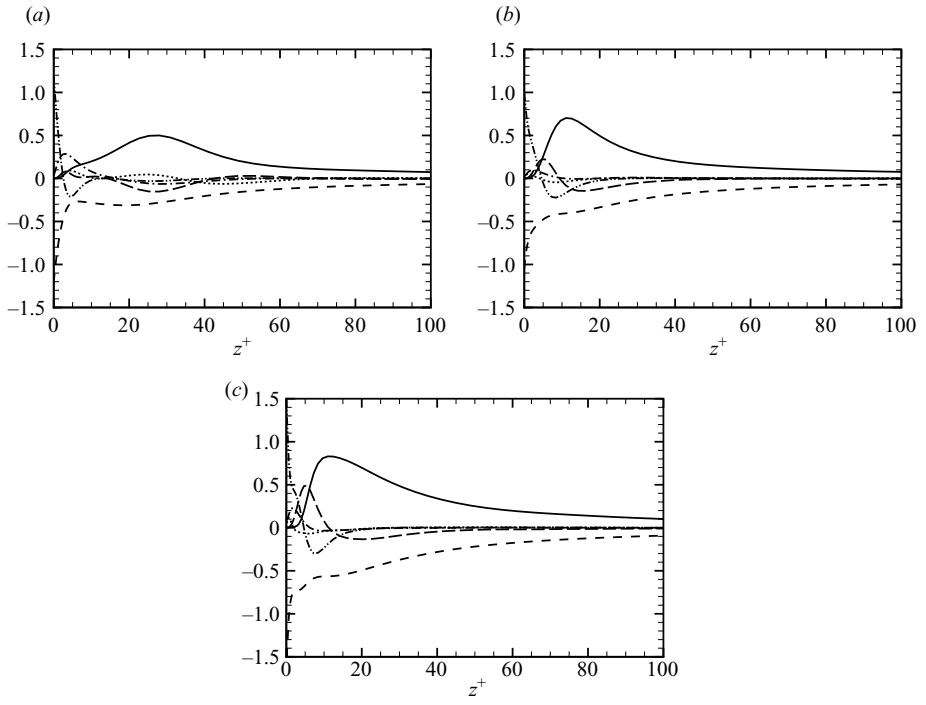

FIGURE 19. Budgets of TKE in turbulence over Airy waves with steepness $ak = 0.25$ and wave ages (*a*) $c/u_* = 2$, (*b*) $c/u_* = 14$ and (*c*) $c/u_* = 25$. Line patterns for budgets are as follows: ·····, advection; ——, production; – · –, pressure transport; – ·· –, viscous diffusion; — —, turbulent transport; – – –, dissipation. All terms are normalized by $100u_*^3/\lambda$.

Calhoun & Street (2001), we normalize all of the terms by $100u_*^3/\lambda$. The TKE budgets for the stationary wavy wall case are consistent with Calhoun & Street (2001) and are not shown here. It is found that for all of the three cases, production and dissipation terms dominate except near the surface where the production term becomes zero and the viscous diffusion term balances the dissipation term. In the current paper, we focus on the effects of surface wave motions on the production term. The effects of wave motions on other TKE budget terms go beyond the scope of the present paper and will be reported in a future work. For $c/u_* = 2$, the peak of the production term is located around $z^+ = 25$, while for $c/u_* = 14$ and 25, the production peaks move towards the surface to around $z^+ = 10$.

The production term in (5.3) can be rewritten as

$$P = \underbrace{P_x^{11} + P_z^{11}}_{P^{11}} + \underbrace{P_x^{33} + P_z^{33}}_{P^{33}}, \tag{5.4}$$

where the superscripts '11' and '33' represent the terms for $(1/2)\langle u'^2\rangle$ and $(1/2)\langle w'^2\rangle$, respectively (there is no production for $(1/2)\langle v'^2\rangle$). Here,

$$\left.\begin{aligned} P_x^{11} &= -\langle u'^2\rangle \frac{\partial\langle u\rangle}{\partial x}\,, \quad P_z^{11} = -\langle u'w'\rangle \frac{\partial\langle u\rangle}{\partial z}\,, \\ P_x^{33} &= -\langle u'w'\rangle \frac{\partial\langle w\rangle}{\partial x}\,, \; P_z^{33} = -\langle w'^2\rangle \frac{\partial\langle w\rangle}{\partial z}\,. \end{aligned}\right\} \tag{5.5}$$

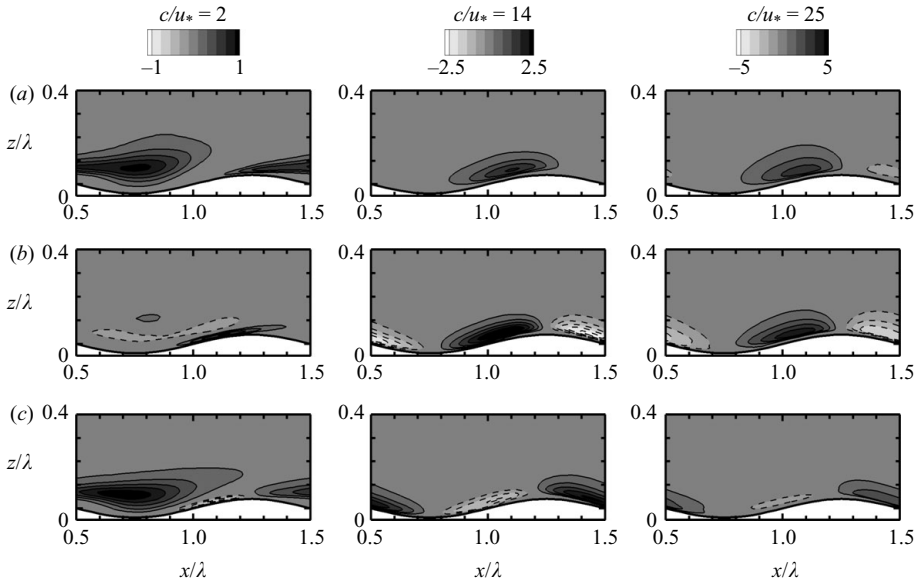

FIGURE 20. The contours of the production term (normalized by $100u_*^3/\lambda$) for $(1/2)\langle u'^2\rangle$ in turbulence over Airy waves with $ak = 0.25$ and $c/u_* = 2$, 14 and 25. (a) Total production $P^{11} = -\langle u'^2\rangle\partial\langle u\rangle/\partial x - \langle u'w'\rangle\partial\langle u\rangle/\partial z$; ($b$) $P_x^{11} = -\langle u'^2\rangle\partial\langle u\rangle/\partial x$; ($c$) $P_z^{11} = -\langle u'w'\rangle\partial\langle u\rangle/\partial z$. The dashed contour lines represent negative values. The surface wave propagates in the $+x$-direction.

For all of the three wave ages, the production terms P_x^{11} and P_z^{11} dominate, while P_x^{33} and P_z^{33} are one order of magnitude smaller. Because of space limitation, the distributions of P_x^{33} and P_z^{33} are not discussed here.

Figure 20 shows the contours of P^{11}, P_x^{11} and P_z^{11} for the case of Airy waves with $ak = 0.25$ and $c/u_* = 2$, 14 and 25. For the case of slow waves, the high-intensity region of P^{11} starts from the wave crest and extends to above the next trough. A comparison between P_x^{11} and P_z^{11} indicates that the contribution of P_z^{11} dominates. The peak of P_z^{11} is located above the wave trough because of the large Reynolds stress $\langle -u'w'\rangle$ (see figure 11a) there. The high-intensity region of P_z^{11} extends further downstream to above the windward side because of the strong shear layer of large $\partial\langle u\rangle/\partial z$ that is indicated by the dense streamwise velocity contour lines in figure 4(d).

The above-given distribution of the production for the slow-wave case is similar to that in the case of turbulence over a stationary wavy wall (see e.g. Calhoun & Street 2001). This implies that when the wave is slow, the surface wave affects the production as well as the TKE mainly by its wavy geometry. As wave age increases, the distribution of the production becomes significantly different from that in the case of a stationary wavy wall.

For the intermediate- and fast-wave cases, the magnitudes of P_x^{11} and P_z^{11} become comparable. Their distributions are similar but with reversed sign. On the windward side of the wave, the term P_x^{11} is positive because $\langle u'^2\rangle > 0$ and $\partial\langle u\rangle/\partial x < 0$ (see figure 13a); the term P_z^{11} is negative because $-\langle u'w'\rangle < 0$ and $\partial\langle u\rangle/\partial z > 0$. The locations of the positive peak of P_x^{11} and the negative peak of P_z^{11} coincide. Because P_x^{11} is larger than P_z^{11}, their combined effect results in a positive peak of P^{11} on the windward side. On the lee side, the term P_x^{11} is negative because $\langle u'^2\rangle > 0$ and $\partial\langle u\rangle/\partial x > 0$; the term P_z^{11} is positive because $-\langle u'w'\rangle > 0$ and $\partial\langle u\rangle/\partial z > 0$. The

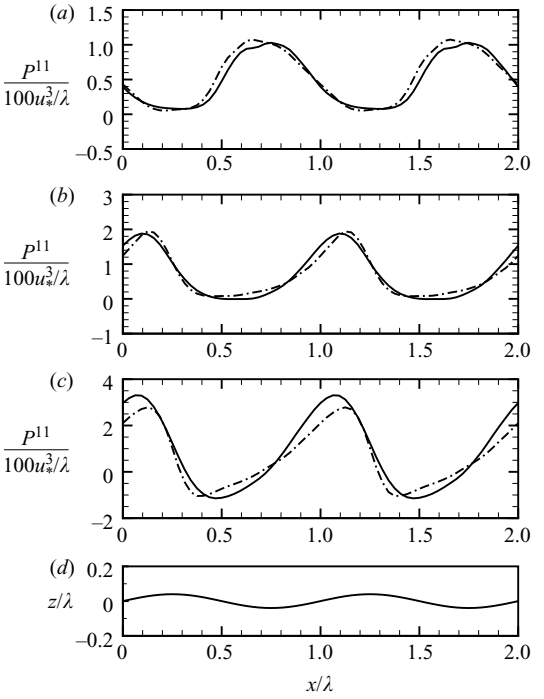

FIGURE 21. Profiles of production P^{11} (normalized by $100u_*^3/\lambda$) above wavy surfaces with steepness $ak = 0.25$ and wave ages (*a*) $c/u_* = 2$, (*b*) $c/u_* = 14$ and (*c*) $c/u_* = 25$: ——, Airy wave; — · —, Stokes wave. For $c/u_* = 2$, the profiles are at the height $(z - \eta)/\lambda = 0.1$; for $c/u_* = 14$ and 25, the profiles are at the height $(z - \eta)/\lambda = 0.05$. The surface wave elevation for the Airy wave case is plotted in (*d*) to indicate the wave phase. The surface wave propagates in the $+x$-direction.

contributions from P_x^{11} and P_z^{11} almost cancel each other and result in a negative peak of P^{11} that is much weaker than the positive peak on the windward side. It is clear that the sign of the total production P^{11} is determined by P_x^{11} for the intermediate- and fast-wave cases. On the windward side of the wave, the large value of $\langle u'^2 \rangle$ results in a large positive value of P_x^{11}, which serves as a large production of $\langle u'^2 \rangle$ itself.

Figure 21 shows the comparison of the production term P^{11} between the Airy wave case and the Stokes case. Similar to the comparison of the Reynolds stress in § 5.2, here we plot the profiles of P^{11} along $(z - \eta)/\lambda = 0.1$ for $c/u_* = 2$ and along $(z - \eta)/\lambda = 0.05$ for $c/u_* = 14$ and 25.

For the case of $(ak, c/u_*) = (0.25, 2)$, the maximum value of P^{11} in the Stokes wave case is slightly larger and shifts upstream compared with that in the Airy wave case. For the case of $(ak, c/u_*) = (0.25, 14)$, the Stokes wave case has a slightly larger maximum value of P^{11}, and the locations of both the maximum and minimum P^{11} shift towards the wave crest compared with the Airy wave case. For the case of $(ak, c/u_*) = (0.25, 25)$, the maximum P^{11} of the Stokes wave case is much smaller than that of the Airy wave case. Similar to the case of $c/u_* = 14$, the locations of both the maximum and minimum P^{11} shift towards the wave crest compared with the Airy wave case.

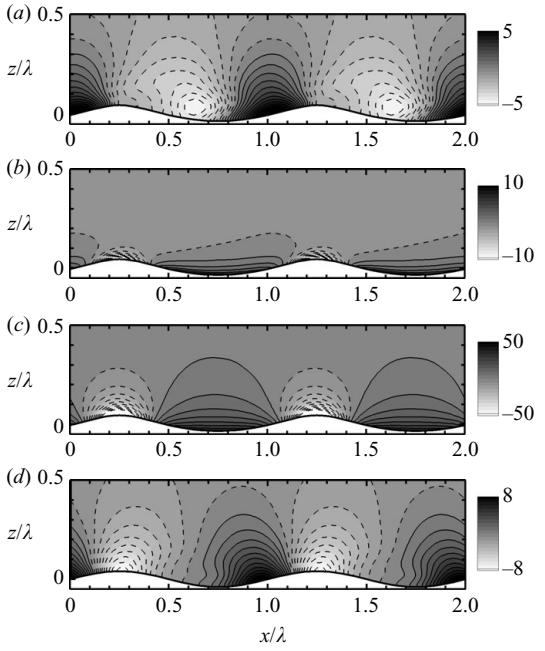

FIGURE 22. The phase-averaged contours of normalized pressure $\langle p \rangle / \rho u_*^2$ for turbulence over Stokes waves with steepness $ak = 0.25$ and wave ages (*a*) $c/u_* = 2$, (*b*) $c/u_* = 14$ and (*c*) $c/u_* = 25$. (*d*) Stationary wavy wall with $ak = 0.25$. The dashed contour lines represent negative values. The contour intervals are 0.5, 1.0, 5.0 and 0.8 in (*a*)–(*d*), respectively. For progressive-wave cases, the surface wave propagates in the $+x$-direction.

The wave nonlinearity effect on the production of TKE shown here is similar to that for the Reynolds stress discussed in § 5.2. A further discussion of the wave nonlinearity effect on the turbulent statistics is given in § 7.

6. Pressure, drag force and wave growth rate

The distribution of the turbulence pressure field near the wavy surface is of special interest to applications including wave growth and attenuation under wind forcing and fish swimming efficiency, among others. Stewart (1970), Donelan (1999) and Makin *et al.* (2007) measured the air flow structure and wave drag for wind over water waves. Sullivan *et al.* (2000) and Kihara *et al.* (2007) studied the dependence of the air pressure field on the wave age for Airy waves with a low steepness $ak = 0.1$. Shen *et al.* (2003) studied the pressure-related form drag and swimming power for the turbulence over a fish-like vertically waving wall with a large steepness $ak = 0.25$. In the present study, the effects of different types of wavy boundary motions with different wave steepness and wave ages are examined in detail.

Figure 22(*a–c*) shows the phase-averaged pressure distribution over Stokes waves with steepness $ak = 0.25$ and wave ages $c/u_* = 2$, 14 and 25, respectively. For comparison, the phase-averaged pressure contours over a stationary wavy wall with $ak = 0.25$ are plotted in figure 22(*d*). It is found that for the case of $(ak, c/u_*) = (0.25, 2)$, the pressure contours are tilted at a short distance above the wave. The high-pressure region is located above the windward side of the wave crest with its peak located on the wave surface. On the other hand, the low-pressure region

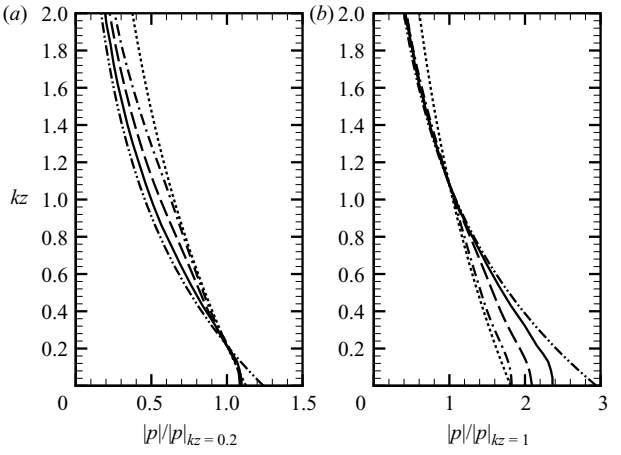

FIGURE 23. Comparison of pressure profiles with exponential decays: ——, the profile of Kudryavtsev *et al.* (2001) estimated by Donelan *et al.* (2006) with $\overline{ak} = 0.05$ and $c/u_* = 3.5$ ($c/U_{10} = 0.13$) (their record LG9); — —, water wave with $(ak, c/u_*) = (0.1, 2)$; — · —, water wave with $(ak, c/u_*) = (0.25, 2)$; — ·· —, $\exp(-kz)$; · · · · ··, $\exp(-0.55kz)$. The profiles are normalized by the pressure amplitude $|p|$ at (*a*) $kz = 0.2$ and (*b*) $kz = 1$, respectively (i.e. assuming that the measurements are conducted at the corresponding heights).

is located between the trough and the leeward side of the crest. As c/u_* increases, the pressure contours become more symmetric about the wave crest and extend further into the bulk flow, almost straight vertically. The high-pressure and low-pressure regions are located right above the wave trough and crest, respectively. These results indicate the influence of strong vertical wave motion on the pressure distribution for relatively fast-moving waves.

The result in figure 22 also indicates that the air pressure in the vicinity of the wave surface is complex, especially for the slow-wave case. For accurate estimation of the surface pressure, Donelan *et al.* (2006) showed the necessity of putting the pressure probe close to the wave surface. In figure 23, we compare the vertical pressure decay profiles of our slow-wave cases with the pressure profile of Kudryavtsev, Makin & Meirink (2001) shown by Donelan *et al.* (2006) with their record LG9. Two exponential profiles, $\exp(-kz)$ and $\exp(-0.55kz)$, are also plotted for comparison. Figure 23 shows that the pressure decay rate decreases as the wave steepness increases. When the measurement is taken at $kz = 0.2$, the surface pressure values from our simulations collapse, and the two exponential extrapolations provide values with about 5 % errors; when the measurement is taken at $kz = 1$ instead, the surface pressure values from our simulations diverge, and the extrapolations can have errors as large as 20 %. This comparison shows the consistency of our results with Kudryavtsev *et al.* (2001). It strongly supports the conclusion by Donelan *et al.* (2006) and confirms the advantage of wave-following pressure probe measurements.

By means of bandpass-filtering and Hilbert transform, Donelan *et al.* (2006) obtained the conditionally phase-averaged surface pressure distribution for a slow-wave case (their record LG9). To validate the pressure distribution in our simulation, we performed an additional simulation with $ak = 0.05$ that matches the mean field condition and compared our phase-averaged surface pressure with their data. As shown in figure 24(*a*), our simulation result agrees well with their measurements.

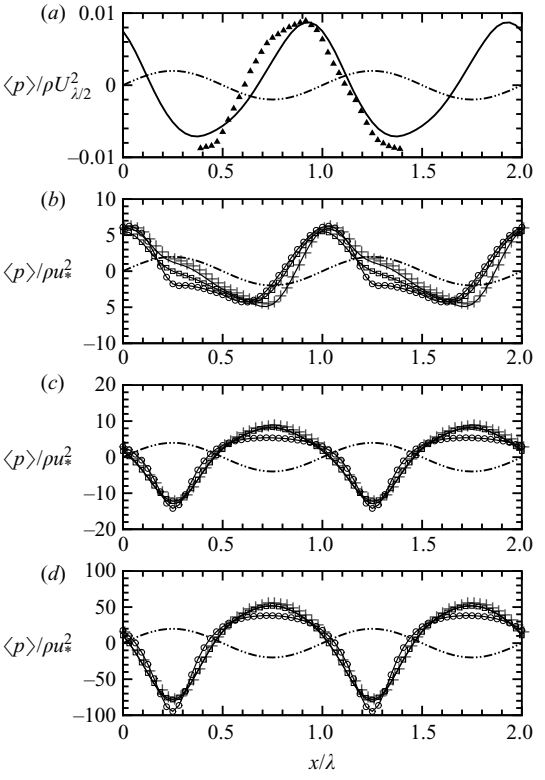

FIGURE 24. Surface pressure distribution for turbulence over water waves. Comparison with experiment for a slow wave with $ak = 0.05$ is shown in (a): ▲, field measurement data of Donelan *et al.* (2006); solid line, current DNS. Results for water waves with $ak = 0.25$ and $c/u_* =$ (a) 2, (b) 14 and (c) 25 are also plotted: —□—, Airy wave; —○—, Stokes wave; —+—, Airy wave with surface drift. The dash-dot-dotted line is the surface elevation of the Airy wave to indicate the wave phase. The surface wave propagates in the $+x$-direction.

Figure 24(b–d) illustrates the effect of wave nonlinearity and surface drift on the surface pressure distribution. Airy waves and Stokes waves with steepness $ak = 0.25$ and wave ages $c/u_* = 2$, 14 and 25 are shown. For the Airy wave case, the wind-induced surface drift effect is also examined. With the surface pressure distribution, the dimensionless form drag per unit area due to pressure is quantified as

$$F_p = \frac{1}{\lambda}\int_0^{\lambda} \frac{\langle p\rangle}{\rho u_*^2}\frac{\mathrm{d}\eta}{\mathrm{d}x}\mathrm{d}x, \tag{6.1}$$

and the wave growth rate parameter introduced by Miles (1957) is obtained as (Li *et al.* 2000)

$$\beta = \frac{2F_p}{(ak)^2}. \tag{6.2}$$

The corresponding form drag and growth rates of the cases in figure 24(b–d) are shown in table 3.

For the slow wave $(ak, c/u_*) = (0.25, 2)$ in figure 24(b), the Stokes wave case has almost the same values for both the maximum and minimum surface pressures as in the Airy wave case. However, because of the steeper crest and the flatter trough, the Stokes wave case has obviously lower surface pressure above the crest and the lee

	Airy wave ($ak = 0.1$)		Airy wave ($ak = 0.25$)		Stokes wave ($ak = 0.25$)		Airy wave with drift ($ak = 0.25$)	
c/u_*	F_p	β	F_p	β	F_p	β	F_p	β
2	0.161	32.29	0.474	15.18	0.540	17.27	0.430	13.76
14	0.005	1.022	−0.010	−0.314	−0.0001	−0.004	−0.009	−0.303
25	−0.044	−8.753	−0.251	−8.048	−0.352	−11.27	−0.265	−8.473

TABLE 3. Form drag and wave growth rate parameter for various wavy boundaries.

side while slightly higher surface pressure above the windward side compared with the Airy wave case. These differences result in about 14 % larger form drag and wave growth rate for the Stokes wave than for the Airy wave as shown in table 3. When the surface drift is considered, the maximum of the surface pressure on the windward side remains almost unchanged compared with the case with no surface drift, while the surface pressure above the crest becomes larger. Meanwhile, the minimum surface pressure becomes smaller and shifts downstream towards the wave trough compared with the case with no surface drift. These differences result in 9 % smaller form drag and wave growth rate (table 3).

For the case of $c/u_* = 14$ and $c/u_* = 25$, because of the larger vertical acceleration on the crest and smaller vertical acceleration on the trough, the surface pressure above the Stokes wave has larger negative peak on the crest and smaller positive peak on the trough compared with the Airy wave case. For the intermediate wave $c/u_* = 14$, the more symmetric distribution of surface pressure results in smaller form drag and growth rate than the slow wave of $c/u_* = 2$ for both the Airy wave and the Stokes wave cases. For the fast wave $c/u_* = 25$, the amplitude of surface pressure becomes over five times larger than the value for $c/u_* = 14$. With a slightly asymmetric distribution of surface pressure around the wave crest, the large magnitude of surface pressure results in larger negative form drag and growth rate than the case of $c/u_* = 14$ (table 3). The amplitudes of the form drag and growth rate for the case of $c/u_* = 25$ are smaller than those for the case of $c/u_* = 2$, in which case the asymmetry of the pressure distribution is much more significant. For $c/u_* = 25$, the amplitude of negative form drag and growth rate for the Stokes wave is about 40 % larger than those for the Airy wave. For both $c/u_* = 14$ and $c/u_* = 25$, the effects of surface drift on surface pressure distribution and consequently on the form drag and growth rate are small because of the small ratio of q_0/c (table 2).

Our DNS result shows that when the wave age increases to the intermediate-wave range, the form drag becomes very small or even negative. This seems to disagree with the measurements or RANS simulations in the literature. This difference is due to the Reynolds number dependence of the pressure distribution and form drag (Mastenbroek 1996; Meirink & Makin 2000). As shown by Sullivan *et al.* (2000), for different Reynolds numbers, the transition points of wave age for the form drag to become zero do not collapse when the wave age is expressed as c/u_*; if the wave age is defined on the basis of a characteristic mean velocity, e.g. $c/U_{\lambda/2}$ or c/U_λ, the convergence can be significantly improved. Here, $U_{\lambda/2}$ and U_λ are respectively the mean horizontal velocities at the heights $z = \lambda/2$ and $z = \lambda$ above the wave surface. The value of $c/U_{\lambda/2}$ is shown in table 4. Our comparison in figure 25 is consistent with the conclusion of Sullivan *et al.* (2000). In figure 25(*b*), the scaling with $c/U_{\lambda/2}$ is shown;

c/u_*	2	14	25
$c/U_{\lambda/2}$	0.13	0.84	1.41

TABLE 4. Values of wave ages for the Airy wave of $ak = 0.1$ discussed in figure 25.

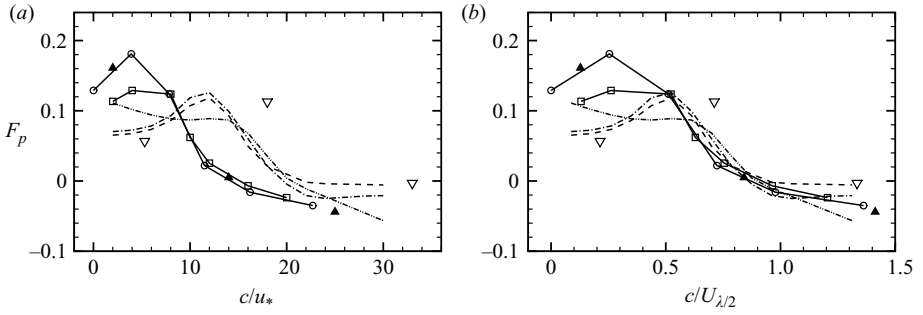

FIGURE 25. Wave-induced form drag for water waves with $ak = 0.1$ as a function of (*a*) c/u_* and (*b*) $c/U_{\lambda/2}$: ▲, current DNS results for Airy waves; —⊖—, DNS results of Sullivan *et al.* (2000); —⊟—, DNS results of Kihara *et al.* (2007); ∇, results of Mastenbroek (1996; also see Mastenbroek *et al.* 1996) with LRR closure scheme. Results of Li *et al.* (2000) with different turbulence closure: — ·· —, $E - \kappa z$; — · —, $q^2 l$; – – –, LRR.

for the scaling with c/U_λ, the result is equally good and is not shown here because of space limitation. Besides the wave age dependence, figure 25 also shows that the peak of the form drag profile shifts towards higher wave age as the Reynolds number increases (the Reynolds number increases as we go from the DNS cases to Li *et al.* 2000 and to Mastenbroek *et al.* 1996). This trend is consistent with the comparison among the DNS, low-Reynolds-number model and high-Reynolds-number model by Meirink & Makin (2000, figure 9).

In table 3, we also compare the form drag and the growth rate parameter for Airy waves with $ak = 0.1$ and 0.25. Because of the smaller steepness, the cases of $ak = 0.1$ have smaller form drag than those for $ak = 0.25$. For the slow wave, the case of $ak = 0.1$ has a growth rate of $\beta = 32.29$, which is larger than the value of $\beta = 15.18$ for $ak = 0.25$. This variation is consistent with the measurements compiled by Peirson & Garcia (2008, figure 6), who showed that the wind-induced growth rate parameter of slow water waves increases as the wave steepness decreases.

To further study the wave steepness effect on the form drag and growth rate parameter, we repeat the simulation of $c/u_* = 2$ with additional ak values and plot the result in figure 26. That is to say in addition to $ak = 0.1$ and 0.25 shown throughout the paper, $ak = 0.01$, 0.025, 0.05, 0.15 and 0.2 are also considered here. Figure 26(*a*) shows that the wave growth rate parameter β, normalized by ρu_*^2 as defined in (6.1) and (6.2), decreases monotonically as ak increases. This is consistent with the data compiled by Peirson & Garcia (2008), which are also plotted in figure 26(*a*) for comparison.

Interestingly, we find that when normalized by $\rho U_{\lambda/2}^2$, the resultant growth rate parameter

$$\beta^{\lambda/2} = \frac{2}{(ak)^2}\frac{1}{\lambda}\int_0^\lambda \frac{\langle p\rangle}{\rho U_{\lambda/2}^2}\frac{\mathrm{d}\eta}{\mathrm{d}x}\mathrm{d}x \tag{6.3}$$

has much less variation, as shown in figure 26(*b*). This suggests that the normalization based on a characteristic mean velocity, e.g. $U_{\lambda/2}$, may help reduce the

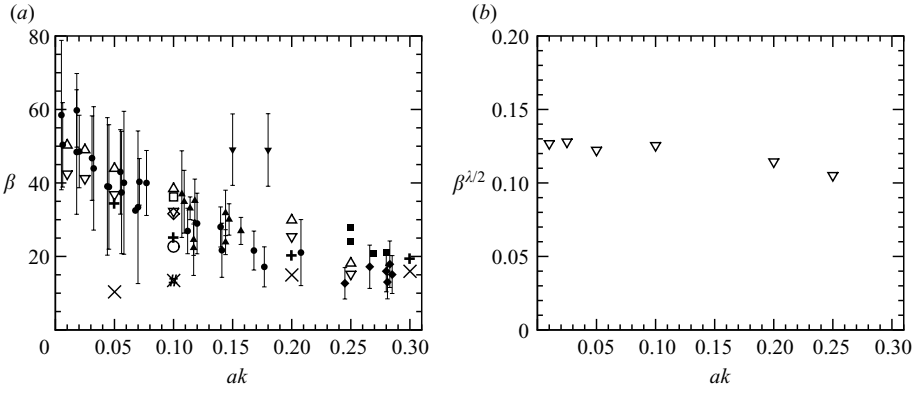

FIGURE 26. Wave growth rate parameter normalized by (*a*) ρu_*^2 and (*b*) $\rho U_{\lambda/2}^2$, plotted as a function of wave steepness. In (*a*), measurement data compiled by Peirson & Garcia (2008) are plotted for comparison and are denoted by the solid symbols with error bars: ▲, Bole (1967); ■, Banner (1990); ▼, Mastenbroek *et al.* (1996); ◆, Banner & Peirson (1998); and ●, Peirson & Garcia (2008). Results from numerical simulations are denoted as follows: ×, RANS result of Mastenbroek (1996) using the LRR model; +, result of Mastenbroek (1996) with the addition of wave-coherent tangential stress contribution (Peirson & Garcia 2008); #, RANS result of Li *et al.* (2000) using the LRR model; □, DNS result of Sullivan *et al.* (2000); ○, DNS result of Kihara *et al.* (2007); ◇, DNS result of Kihara *et al.* (2007) with wave-coherent tangential stress contribution taken into account; ▽, the present DNS result; △, the present DNS result with wave-coherent tangential stress contribution taken into account. For the present DNS results, $c/u_* = 2$. For data from the literature, cases with c/u_* values in the neighbourhood of 2 are selected here.

steepness-induced variation of the growth rate parameter for the slow-wave case. Recall that in figure 25, the use of $U_{\lambda/2}$ in the definition of wave age helps the results from different simulations to collapse. The above results suggest the advantage of using the large-scale mean velocity at a height comparable to the wavelength (e.g. $U_{\lambda/2}$ or U_λ) as the characteristic velocity scale over using the friction velocity u_*. To further obtain a comprehensive understanding of this problem, additional simulations and more analyses are required.

At $ak = 0.1$, figure 26(*a*) shows that the β value obtained from our DNS falls between the values obtained from the DNS studies by Sullivan *et al.* (2000) and Kihara *et al.* (2007). However, the β values from RANS studies, using the LRR model, by Mastenbroek (1996) and Li *et al.* (2000) are lower than the DNS results, despite the fact that kinematic similarities are obtained between the present DNS and the RANS simulation by Mastenbroek (1996) (cf. figure 10).

The recent finding by Peirson & Garcia (2008) provides a possible approach to reduce the discrepancy in β values. If the contribution of tangential stress is taken into account, the β values from the numerical model increase to be closer to the measurement data. The tangential surface stress contributes to the wave growth through its coherence with the wave surface tangential velocity u_t. The corresponding dimensionless surface drag per unit area is given as

$$F_{wc} = \frac{1}{c\lambda}\int_0^\lambda \frac{\langle\tau_s\rangle}{\rho u_*^2} u_t \frac{1}{(\eta_x^2+1)^{1/2}}(\eta_x^2+1)^{1/2}\mathrm{d}x$$
$$= \frac{1}{c\lambda}\int_0^\lambda \frac{\nu}{u_*^2}\frac{1}{(\eta_x^2+1)^{3/2}}\left(\left(1-\eta_x^2\right)\left(\frac{\partial\langle u\rangle}{\partial z}+\frac{\partial\langle w\rangle}{\partial x}\right)+2\eta_x\left(\frac{\partial\langle w\rangle}{\partial z}-\frac{\partial\langle u\rangle}{\partial x}\right)\right)$$
$$\times (u_s - \eta_x w_s)\mathrm{d}x. \tag{6.4}$$

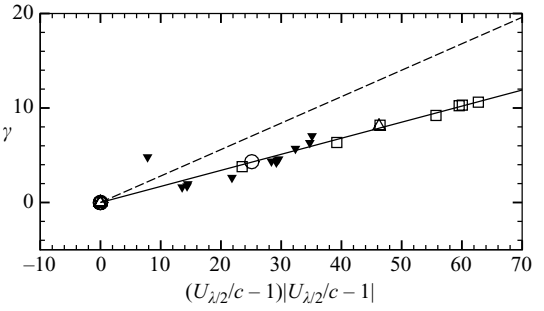

FIGURE 27. Comparison of temporal growth rate γ with Donelan *et al.* (2006): ——, their parameterization $\gamma = 0.17(U_{\lambda/2}/c-1)|U_{\lambda/2}/c-1|$; ▼, their hindcast estimates based on the data of Donelan (1999); – – –, parameterization of Donelan (1999) $\gamma = 0.28(U_{\lambda/2}/c-1)|U_{\lambda/2}/c-1|$. The results of the current simulation are denoted by the open symbols: □, Airy wave with various steepness; △, Airy wave with $ak = 0.25$; ○, Stokes wave with $ak = 0.25$.

When F_{wc} is added to F_p (cf. (6.2)), figure 26(a) shows that the difference in the corresponding values of β between the DNS and the LRR model of Mastenbroek (1996) reduces significantly. The agreement with the measurement values is improved. (The wave-coherent tangential stress was not reported in Sullivan *et al.* 2000 and Li *et al.* 2000, and therefore the corresponding modified values of β are not shown here.) The above improvement is furthermore obtained for other wave steepness, with a more significant effect in low-ak cases, for which the contribution from the wave-coherent tangential stress is more important (Peirson & Garcia 2008).

Furthermore, as discussed by Belcher & Hunt (1998), many factors, such as the Reynolds number, the variation of surface roughness and the turbulence models, can affect the pressure distribution and the corresponding value of β. To study these effects, systematic simulations using LES of air–water coupled flow for a wide range of Reynolds number may provide a useful tool. This goes beyond the scope of the current paper and will be investigated in our future study.

Under the wind pressure forcing, the temporal growth rate of a water wave with angular frequency ω (cf. Donelan *et al.* 2006) can be obtained as

$$\gamma = \frac{\rho_w}{\rho_a}\frac{1}{\omega E(\omega)}\frac{\partial E(\omega)}{\partial t} = \left(\frac{u_*}{c}\right)^2 \beta \,, \tag{6.5}$$

where $E = \rho_w g a^2/2$ is the wave energy and ρ_w and ρ_a are the water and air densities, respectively. The dependence of γ on the inverse wave age $U_{\lambda/2}/c$ is estimated as

$$\gamma = S_{\lambda/2}(U_{\lambda/2}/c-1)|U_{\lambda/2}/c-1| \,, \tag{6.6}$$

where $S_{\lambda/2}$ is the sheltering coefficient. Donelan & Pierson (1987) obtained $S_{\lambda/2} = 0.19$ from electromagnetic microwave-scattering field measurements. Based on laboratory measurements, Donelan (1999) obtained $S_{\lambda/2} = 0.28$. Donelan *et al.* (2006) further improved this parameterization by using wave-follower field measurement data and showed that $S_{\lambda/2} = 0.17$. The comparison in figure 27 shows that our DNS result agrees very well with Donelan *et al.* (2006) and supports their improvement in the parameterization.

Peirson & Garcia (2008) compiled the data from various measurements. In figure 28, we compare the present DNS result with the data. The values from the parameterizations by Donelan & Pierson (1987), Donelan (1999) and Donelan *et al.*

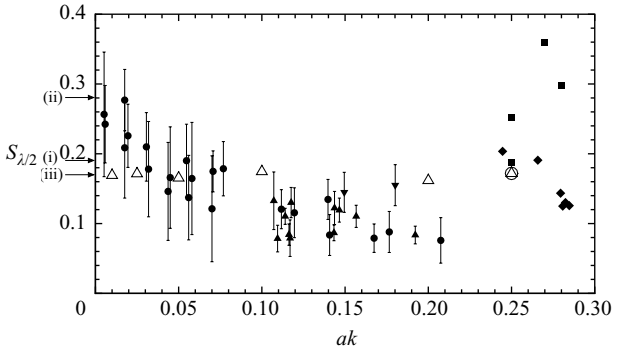

FIGURE 28. Comparison of steepness dependence of sheltering coefficient at half-wavelength height above wave surface. The data compiled by Peirson & Garcia (2008) are denoted by the solid symbols with the error bars: ▲, Bole (1967); ■, Banner (1990); ▼, Mastenbroek *et al.* (1996); ◆, Banner & Peirson (1998); and ●, Peirson & Garcia (2008). The results of slow-wave cases in the present study are denoted by the open symbols: △, Airy wave; ○, Stokes wave. Parameterizations based on measurement data are indicated: (i) $S_{\lambda/2} = 0.19$, Donelan & Pierson (1987); (ii) $S_{\lambda/2} = 0.28$, Donelan (1999); and (iii) $S_{\lambda/2} = 0.17$, Donelan *et al.* (2006).

(2006) are also indicated in the figure. It should be noted that these parameterizations were obtained on the basis of the measurement data for waves with steepness less than those from Banner (1990) and Banner & Peirson (1998) shown in figure 28. The applicable wave steepness for these parameterizations was not reported explicitly in the original studies.

Figure 28 indicates that our DNS result agrees with the parameterization by Donelan *et al.* (2006) with the 0.17 sheltering coefficient. The present DNS result also falls in the range of the measurement data. However, the measurement data by Peirson & Garcia (2008) indicate variations in the sheltering coefficient as the wave steepness increases, while the present DNS shows an almost-constant sheltering coefficient. This difference may be partially due to the difference in the wave age values (in figure 28, c/u_* is always 2 in our simulation, while it varies in Peirson & Garcia 2008). It may also be caused by the difference in the wave conditions. For example, as the steepness of a slow wave increases, the nonlinearity of the wave shape increases, the asymmetry of the waveform becomes more significant, and the variation of the surface roughness changes; for very large steepness, wave breaking happens (e.g. the data from Banner 1990). Some of these effects go beyond the capability of the present DNS using prescribed wave boundary conditions. To study their influence, an air–water coupled simulation is required.

We also compared β and γ (as functions of c/u_*) obtained from our DNS with existing simulations and theories, as well as the measurements compiled by Plant (1982) (not shown). Our result is consistent with the existing simulations and theories. However, for β there exists large scattering in the measurement data. The numerical results fall into the range of the measurement data but are close to their lower bound. As pointed out by Belcher & Hunt (1998), although much progress has been made in the model development, there still exists a difference between the prediction and the measurement, and additional research effort is required. As shown earlier, the inclusion of wave-coherent tangential stress helps reduce the difference (Peirson & Garcia 2008).

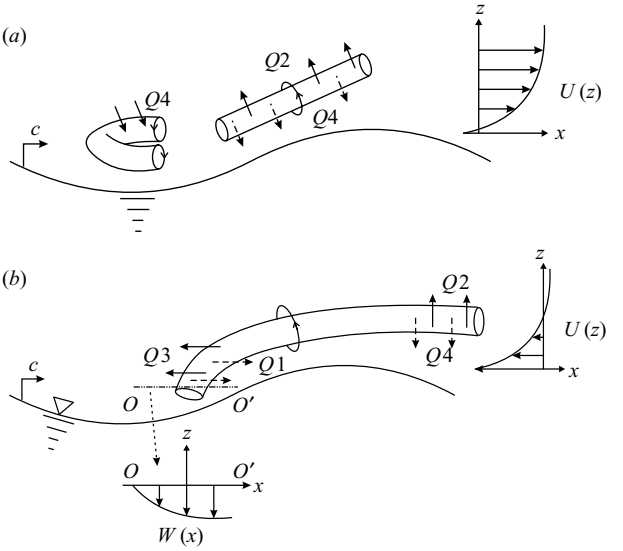

FIGURE 29. Sketch of coherent vortical structures over (*a*) slow and (*b*) fast waves.

7. Discussion and conclusions

In the present study, DNS has been performed for turbulent flows over various wavy boundaries, including stationary wavy walls, vertically waving walls, Airy waves and Stokes waves. Effects of various surface wave features have been considered, including wave steepness, wave age, wave nonlinearity and wind-induced surface drift. Through systematic simulations with detailed near-surface flow structures well resolved, we have investigated effects of different boundary waving motions on the turbulent flow.

The surface wave boundary condition consists of both geometric and kinematic features. The geometry of the wave surface provides periodically varying surface curvature and alternating pressure gradients that affect the turbulent flow above it. The horizontal and vertical motions of the surface wave provide direct distortion to the velocity field of the turbulent flow.

Turbulent flow structure is found to be strongly dependent on wave age. For a slow wave $c/u_* = 2$, the geometric effect of the surface wave on turbulence dominates. The distribution of turbulence statistics including Reynolds stress and TKE is similar to that over a stationary wavy wall. Our investigation suggests that above the slow wave, there exist two types of coherent vortical structures, namely quasi-streamwise vortices and horseshoe vortices, as shown in figure 29(*a*). The horseshoe vortices are usually located near the wave trough. The quasi-streamwise vortices are often located near the windward side of the wave crest; and some of them extend over the crest and lift above the next trough. Since the surface motion of the slow wave is small, the turbulence velocity field is dominated by the shear of the streamwise velocity $U(z)$ over the wavy surface, i.e. geometric constraint. The horseshoe vortices have their heads on the upstream side, while their legs are on the downstream side. The head has $\omega_y > 0$ that is consistent with the vorticity induced by the mean shear $U(z)$. The rotation of the head and the counter-rotating motions of the two legs induce a downwelling motion of the fluid on the inner side of the horseshoe. Because of the mean shear profile $U(z)$, this downwelling motion results in a sweep event ($Q4$) of high-speed

fluid towards the wave boundary. The quasi-streamwise vortices on the windward side of the crest have either positive or negative ω_x. The quasi-streamwise vortices often appear individually, rather than as counter-rotating pairs. For a quasi-streamwise vortex with $\omega_x < 0$, when observed along the streamwise direction, its rotating motion results in an upwelling motion on the right side and a downwelling motion on the left side. Because of the mean shear profile $U(z)$, the vortex is associated with an ejection event ($Q2$) on its right side and a sweep event ($Q4$) on its left side. A quasi-streamwise vortex with $\omega_x > 0$ has similar effects but with the locations of $Q2$ and $Q4$ switched.

For the intermediate wave $c/u_* = 14$ and fast wave $c/u_* = 25$, the kinematic effect of the surface wave on turbulence dominates the geometric effect. For these two cases, the wave motions are large, and the horizontal profile of the wave-induced vertical velocity $W(x)$ becomes comparable to that of $U(z)$ (see figure 29*b*). In both cases, the quasi-streamwise vortices dominate near the wave surface. A sketch of the coherent vortical structures over a fast wave is shown in figure 29(*b*). These vortices start from the windward side and extend over the crest. They tend to bend to follow the curvature of the wave. On the windward side, the upstream end of a quasi-streamwise vortex tilts towards the vertical direction. For a vortex with $\omega_x < 0$, this tilting results in a vertical vorticity component $\omega_z < 0$. When observed along the streamwise direction, the rotation of the upstream end causes a counter-streamwise motion of fluid on its right side and a streamwise motion of fluid on its left side. With the shear profile $W(x)$ along O–O' as shown in figure 29(*b*), the rotation of the upstream end results in a $Q3$ event on its right side and a $Q1$ event on its left side. When the vortex extends over the crest, its downstream end reaches the leeward side of the crest and turns towards the horizontal direction. The rotation of the downstream end of the vortex with $\omega_x < 0$ causes an upwelling motion on its right side and a downwelling motion on its left side. Because of the mean shear profile $U(z)$, this results in a $Q2$ event on the right side and a $Q4$ event on the left side. Near the crest, the effects of ω_x and ω_z cancel each other. The situation for a quasi-streamwise vortex with $\omega_x > 0$ is similar but with the locations switched between $Q1$ and $Q3$ and between $Q2$ and $Q4$. More details on the characteristics of the coherent vortical structures are given in Yang & Shen (2009).

Besides the wave age dependence, the effect of surface waves on the turbulence structures also depends on the wave steepness ak. The larger ak is, the more the wave influences distributions of turbulent quantities, and the further the influence extends into the bulk flow.

The surface wave nonlinearity effect, though not as strong as wave steepness and wave age effects, still has an appreciable influence on the turbulence above water waves. A summary of this surface wave nonlinearity effect on turbulence is shown in figure 30. For the slow wave $c/u_* = 2$, the geometric effect of the surface wave dominates. The Stokes wave has a steeper crest that is higher and narrower than the crest of the Airy wave. This results in an increase in the intensity of turbulence quantities (e.g. Reynolds stress and TKE) and a phase shift of their distributions towards the upstream crest. For $c/u_* = 14$ and 25, the kinematic effect of the surface wave dominates the geometric effect. The vertical velocity of the Stokes wave has a smaller amplitude, and the peaks on both sides of the wave crest shift towards the crest. This results in a reduction in the intensity of turbulence quantities and a phase shift of their distributions towards the crest from both sides.

The effect of wind-induced surface drift on turbulence is important only for the slow-wave case of $c/u_* = 2$, where the ratio of the mean drift speed to the wave phase speed is $q_0/c = 0.275$. The presence of the surface drift results in a reduction in the

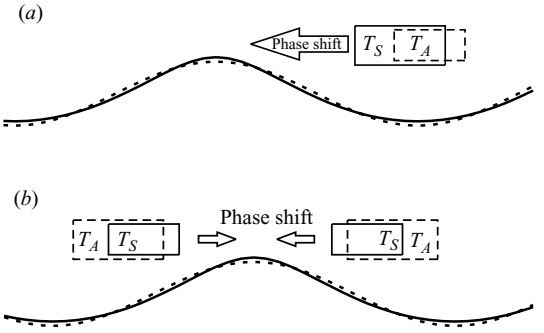

FIGURE 30. Sketch of wave nonlinearity effect on turbulence structures over (*a*) slow and (*b*) intermediate and fast waves. The solid lines represent the properties for the Stokes wave case, while the dashed lines represent the properties for the Airy wave case; T_S represents the turbulent quantities for the Stokes wave case; T_A represents the turbulent quantities for the Airy wave case. The sizes of T_S and T_A represent their relative magnitudes.

Reynolds stress and a phase shift of the high-Reynolds-stress region in the downstream direction. This intensity reduction and phase shift further affect other turbulence quantities such as turbulence intensity and production of TKE. For $c/u_* = 14$ and 25, the influence of surface drift on turbulence structure is negligible because the value of q_0/c is small.

The unique features of coherent vortical structures near the wave surface observed in the current study and the key role these vortices play in momentum transport suggest the importance of further study in this area. A better understanding of the physical process may lead to improved turbulence modelling. For example, LES at high Reynolds numbers requires wall-layer models to relate the shear stress to flow quantities. Knowledge of vortical structures may be used to construct such models (see e.g. Piomelli *et al.* 1989).

For the problem of wind–wave interaction, air flow separation may play an important role in steep waves. In the present study, no apparent separation in the mean flow is observed. Our investigation of the instantaneous flow field indicates that instantaneous flow separations happen intermittently around the lee side and the trough of the surface wave. The present result is compared with the field measurements by Donelan *et al.* (2006) at Lake George in Australia. It should be noted that in the measurements, the waves are in a transitional water depth condition, which results in stronger nonlinearity effects than the case of prescribed deep-water waves in the present study. As a result, the size and intensity of the instantaneous separation in the present study is smaller than the full separation shown by Donelan *et al.* (2006). To extend our turbulence simulation capability to the study of air flow separation over steeper waves, we have been developing alternative approaches with air and water motions dynamically coupled that provide more realistic interface boundary conditions and waveforms (e.g. sharper and asymmetric at the wave crest). This flow separation problem is currently being studied by our group.

Based on our DNS data, pressure-induced form drag and wave growth rate have been calculated. The values are consistent with existing measurement data and agree with other numerical results. Our simulation indicates that wave nonlinearity can have an appreciable impact on form drag and wave growth rate. This finding suggests the importance of including realistic wave dynamics, rather than using simple wave

theory, in the study of wind–wave interaction. In numerical studies, coupled simulation of wind and wave motions is desirable. This is a subject of our ongoing research.

This research is supported by the Office of Naval Research. The Young Investigator award to LS is gratefully acknowledged. We would like to thank the referees for their valuable comments that provided us significant help to improve the previous version of this paper.

REFERENCES

Adrian, R. J. 2007 Hairpin vortex organization in wall turbulence. *Phys. Fluids* **19**, 041301.

Adrian, R. J., Meinhart, C. D. & Tomkins, C. D. 2000 Vortex organization in the outer region of the turbulent boundary layer. *J. Fluid Mech.* **422**, 1–54.

Al-Zanaidi, M. A. & Hui, W. H. 1984 Turbulent airflow over water waves – a numerical study. *J. Fluid Mech.* **148**, 225–246.

Babanin, A. V., Banner, M. L., Young, I. R. & Donelan, M. A. 2007 Wave-follower field measurements of the wind-input spectral function. Part III. Parameterization of the wind-input enhancement due to wave breaking. *J. Phys. Oceanogr.* **37**, 2764–2775.

Banner, M. L. 1990 The influence of wave breaking on the surface pressure distribution in wind–wave interactions. *J. Fluid Mech.* **211**, 463–495.

Banner, M. L. & Melville, W. K. 1976 On the separation of air flow over water waves. *J. Fluid Mech.* **77**, 825–842.

Banner, M. L. & Peirson, W. L. 1998 Tangential stress beneath wind-driven air–water interface. *J. Fluid Mech.* **364**, 115–145.

Banner, M. L. & Phillips, O. M. 1974 On the incipient breaking of small scale waves. *J. Fluid Mech.* **65**, 647–656.

Belcher, S. E. & Hunt, J. C. R. 1993 Turbulent shear flow over slowly moving waves. *J. Fluid Mech.* **251**, 109–148.

Belcher, S. E. & Hunt, J. C. R. 1998 Turbulent flow over hills and waves. *Annu. Rev. Fluid Mech.* **30**, 507–538.

Bole, J. B. 1967 Response of gravity water waves to wind excitation. PhD thesis, Department of Civil Engineering, Stanford University, Palo Alto, CA.

Calhoun, R. J. & Street, R. J. 2001 Turbulent flow over a wavy surface: neutral case. *J. Geophys. Res.* **106**, 9277–9293.

Chakraborty, P., Balachandar, S. & Adrian, R. J. 2005 On the relationships between local vortex identification schemes. *J. Fluid Mech.* **535**, 189–214.

Cherukat, P., Na, Y., Hanratty, T. J. & McLaughlin, J. B. 1998 Direct numerical simulation of a fully developed turbulent flow over a wavy wall. *Theoret. Comput. Fluid Dyn.* **11**, 109–134.

Choi, H., Moin, P. & Kim, J. 1992 Direct numerical simulation of turbulent flow over riblets. *CTR Manuscript* 137. Center for Turbulence Research, Stanford University.

Cohen, J. E. & Belcher, S. E. 1999 Turbulent shear flow over fast-moving waves. *J. Fluid Mech.* **386**, 345–371.

De Angelis, V., Lombardi, P. & Banerjee, S. 1997 Direct numerical simulation of turbulent flow over a wavy wall. *Phys. Fluids* **9**, 2429–2442.

Dommermuth, D. G. & Yue, D. K. P. 1987 A high-order spectral method for the study of nonlinear gravity waves. *J. Fluid Mech.* **184**, 267–288.

Donelan, M. A. 1999 Wind-induced growth and attenuation of laboratory waves. In *Wind-Over-Wave Couplings: Perspectives and Prospects* (ed. S. G. Aajjadi, N. H. Thomas & J. C. R. Hunt), pp. 183–194. Clarendon.

Donelan, M. A., Babanin, A. V., Young, I. R. & Banner, M. L. 2006 Wave-follower field measurements of the wind-input spectral function. Part II. Parameterization of the wind input. *J. Phys. Oceanogr.* **36**, 1672–1689.

Donelan, M. A., Babanin, A. V., Young, I. R., Banner, M. L. & McCormick, C. 2005 Wave-follower field measurements of the wind-input spectral function. Part I. Measurements and calibrations. *J. Atmos. Ocean. Technol.* **22**, 799–813.

Donelan, M. A., Haus, B. K., Reul, N., Plant, W. J., Stiassnie, M., Graber, H. C., Brown, O. B. & Saltzman, E. S. 2004 On the limiting aerodynamic roughness of the ocean in very strong winds. *Geophys. Res. Lett.* **31**, L18306.

Donelan, M. A. & Pierson, W. J. 1987 Radar scattering and equilibrium ranges in wind-generated waves with application to scatterometry. *J. Geophys. Res.* **92** (C5), 4971–5029.

Donelan, M. A. & Plant, W. J. 2009 A threshold for wind-wave growth. *J. Geophys. Res.* **114**, C07012.

Fabrikant, A. L. 1976 Quasilinear theory of wind-wave generation. *Izv. Atmos. Ocean. Phys.* **12**, 524–526.

Gent, P. R. & Taylor, P. A. 1976 A numerical model of the air flow above water waves. *J. Fluid Mech.* **77**, 105–128.

Gent, P. R. & Taylor, P. A. 1977 A note on 'separation' over short wind waves. *Boundary-Layer Met.* **11**, 65–87.

Gong, W., Taylor, P. A. & Dörnbrack, A. 1996 Turbulent boundary-layer flow over fixed aerodynamically rough two-dimensional sinusoidal waves. *J. Fluid Mech.* **312**, 1–37.

Günther, A. & von Rohr, P. R. 2003 Large-scale structures in a developed flow over a wavy wall. *J. Fluid Mech.* **478**, 257–285.

Harlow, F. H. & Welch, J. E. 1965 Numerical calculation of time-dependent viscous incompressible flow of fluid with free surface. *Phys. Fluids* **8**, 2182–2189.

Henn, D. S. & Sykes, R. I. 1999 Large-eddy simulation of flow over wavy surfaces. *J. Fluid Mech.* **383**, 75–112.

Hristov, T. S., Miller, S. D. & Friehe, C. A. 2003 Dynamical coupling of wind and ocean waves through wave-induced air flow. *Nature* **422**, 55–58.

Hsu, C.-T., Hsu, E. Y. & Street, R. L. 1981 On the structure of turbulent flow over a progressive water wave: theory and experiment in a transformed, wave-following coordinate system. *J. Fluid Mech.* **105**, 87–117.

Hsu, C.-T., Wu, H.-Y., Hsu, E.-Y. & Street, R. L. 1982 Momentum and energy transfer in wind generation of waves. *J. Phys. Oceanogr.* **12**, 929–951.

Hudson, J. D. 1993 The effect of a wavy boundary on a turbulent flow. PhD thesis, University of Illinois, Urbana, IL.

Hudson, J. D., Dykhno, L. & Hanratty, T. J. 1996 Turbulence production in flow over a wavy wall. *Exps. Fluids* **20**, 257–265.

Hunt, J. C. R., Leibovich, S. & Richards, K. J. 1988 Turbulent shear flows over low hills. *Q. J. R. Met. Soc.* **114**, 1435–1470.

Hussain, A. K. M. F. & Reynolds, W. C. 1970 The mechanics of an organized wave in turbulent shear flow. *J. Fluid Mech.* **41**, 241–281.

Janssen, P. A. E. M. 1982 Quasilinear approximation for the spectrum of wind-generated water waves. *J. Fluid Mech.* **117**, 493–506.

Jeffreys, H. 1925 On the formation of water waves by wind. *Proc. R. Soc. Lond.* A **107**, 189–206.

Jeong, J. & Hussain, F. 1995 On the identification of a vortex. *J. Fluid Mech.* **285**, 69–94.

Jeong, J., Hussain, F., Schoppa, W. & Kim, J. 1997 Coherent structures near the wall in a turbulent channel flow. *J. Fluid Mech.* **332**, 185–214.

Kihara, N., Hanazaki, H., Mizuya, T. & Ueda, H. 2007 Relationship between airflow at the critical height and momentum transfer to the traveling waves. *Phys. Fluids* **19**, 015102.

Kim, J. 1983 On the structure of wall-bounded turbulent flows. *Phys. Fluids* **26**, 2088–2097.

Kim, J. & Moin, P. 1985 Application of a fractional-step method to incompressible Navier–Stokes equations. *J. Comput. Phys.* **59**, 308–323.

Kim, J., Moin, P. & Moser, R. 1987 Turbulence statistics in fully developed channel flow at low Reynolds number. *J. Fluid Mech.* **177**, 133–166.

Krettenauer, K. & Schumann, U. 1992 Numerical simulation of turbulent convection over wavy terrain. *J. Fluid Mech.* **237**, 261–299.

Kruse, N., Günther, A. & von Rohr, P. R. 2003 Dynamics of large-scale structures in turbulent flow over a wavy wall. *J. Fluid Mech.* **485**, 87–96.

Kudryavtsev, V. N., Makin, V. K. & Meirink, J. F. 2001 Simplified model of the air flow above the waves. *Boundary-Layer Met.* **100**, 63–90.

LI, P. Y., XU, D. & TAYLOR, P. A. 2000 Numerical modelling of turbulent airflow over water waves. *Boundary-Layer Met.* **95**, 397–425.

LIGHTHILL, M. J. 1962 Physical interpretation of the mathematical theory of wave generation by wind. *J. Fluid Mech.* **14**, 385–398.

LIN, M.-Y., MOENG, C.-H., TSAI, W.-T., SULLIVAN, P. P. & BELCHER, S. E. 2008 Direct numerical simulation of wind-wave generation processes. *J. Fluid Mech.* **616**, 1–30.

MAASS, C. & SCHUMANN, U. 1994 Numerical simulation of turbulent flow over a wavy boundary. *Direct Large-Eddy Sim.* **1**, 287–297.

MAAT, N. & MAKIN, V. K. 1992 Numerical simulation of air flow over breaking waves. *Boundary-Layer Met.* **60**, 77–93.

MAKIN, V. K., BRANGER, H., PEIRSON, W. L. & GIOVANANGELI, J. P. 2007 Stress above wind-plus-paddle waves: modelling of a laboratory experiment. *J. Phys. Oceanogr.* **37**, 2824–2837.

MAKIN, V. K. & KUDRYAVTSEV, V. N. 2002 Impact of dominant waves on sea drag. *Boundary-Layer Met.* **103**, 83–99.

MAKIN, V. K., KUDRYAVTSEV, V. N. & MASTENBROEK, C. 1995 Drag of the sea surface. *Boundary-Layer Met.* **79**, 159–182.

MASTENBROEK, C. 1996 Wind–wave interaction. PhD thesis, Delft University of Technology, Delft, The Netherlands.

MASTENBROEK, C., MAKIN, V. K., GARAT, M. H. & GIOVANANGELI, J. P. 1996 Experimental evidence of the rapid distortion of turbulence in the air flow over water waves. *J. Fluid Mech.* **318**, 273–302.

MEIRINK, J. F. & MAKIN, V. K. 2000 Modelling low-Reynolds-number effects in the turbulent air flow over water waves. *J. Fluid Mech.* **415**, 155–174.

MILES, J. W. 1957 On the generation of surface waves by shear flows. *J. Fluid Mech.* **3**, 185–204.

MOIN, P. & KIM, J. 1985 The structure of the vorticity field in turbulent channel flow. Part 1. Analysis of instantaneous fields and statistical correlations. *J. Fluid Mech.* **155**, 441–464.

MOIN, P. & MAHESH, K. 1998 Direct numerical simulation: a tool in turbulence research. *Annu. Rev. Fluid Mech.* **30**, 539–578.

NAKAGAWA, S. & HANRATTY, T. J. 2001 Particle image velocimetry measurements of flow over a wavy wall. *Phys. Fluids* **13**, 3504–3507.

NAKAGAWA, S., NA, Y. & HANRATTY, T. J. 2003 Influence of a wavy boundary on turbulence. Part I. Highly rough surface. *Exps. Fluids* **35**, 422–436.

PEIRSON, W. & GARCIA, A. W. 2008 On the wind-induced growth of slow water waves of finite steepness. *J. Fluid Mech.* **608**, 243–274.

PHILLIPS, O. M. 1957 On the generation of waves by turbulent wind. *J. Fluid Mech.* **2**, 417–445.

PHILLIPS, O. M. & BANNER, M. L. 1974 Wave breaking in the presence of wind drift and swell. *J. Fluid Mech.* **66**, 625–640.

PIOMELLI, U., FERZIGER, J., MOIN, P. & KIM, J. 1989 New approximate boundary conditions for large eddy simulations of wall-bounded fows. *Phys. Fluids* A **1**, 1061–1068.

PLANT, W. J. 1982 A relationship between wind stress and wave slope. *J. Geophys. Res.* **87**, 1961–1967.

REUL, N., BRANGER, H. & GIOVANANGELI, J.-P. 1999 Air flow separation over unsteady breaking waves. *Phys. Fluids* **11**, 1959–1961.

REUL, N., BRANGER, H. & GIOVANANGELI, J.-P. 2008 Air flow structure over short-gravity breaking water waves. *Boundary-Layer Met.* **126**, 477–505.

ROBINSON, S. K. 1991 Coherent motions in the turbulent boundary layer. *Annu. Rev. Fluid Mech.* **23**, 601–639.

SCHWARTZ, L. W. 1974 Computer extension and analytic continuation of Stokes' expansion for gravity waves. *J. Fluid Mech.* **62**, 553–578.

SHAIKH, N. & SIDDIQUI, K. 2008 Airside velocity measurements over the wind-sheared water surface using particle image velocimetry. *Ocean Dyn.* **58**, 65–79.

SHEN, L., ZHANG, X., YUE, D. K. P. & TRIANTAFYLLOU, M. S. 2003 Turbulent flow over a flexible wall undergoing a streamwise travelling wave motion. *J. Fluid Mech.* **484**, 197–221.

SNYDER, R. L., DOBSON, F. W., ELLIOTT, J. A. & LONG, R. B. 1981 Array measurements of atmospheric pressure fluctuations above surface gravity waves. *J. Fluid Mech.* **102**, 1–59.

Stewart, R. H. 1970 Laboratory studies of the velocity field over deep-water waves. *J. Fluid Mech.* **42**, 733–754.

Sullivan, P. P., Edson, J. B., Hristov, T. & McWilliams, J. C. 2008 Large-eddy simulations and observations of atmospheric marine boundary layers above nonequilibrium surface waves. *J. Atmos. Sci.* **65**, 1225–1245.

Sullivan, P. P., McWilliams, J. C. & Moeng, C.-H. 2000 Simulation of turbulent flow over idealized water waves. *J. Fluid Mech.* **404**, 47–85.

Taneda, S. & Tomonari, Y. 1974 An experiment on the flow around a waving plate. *J. Phys. Soc. Japan* **36**, 1683–1689.

Triantafyllou, M. S., Triantafyllou, G. S. & Yue, D. K. P. 2000 Hydrodynamics of fishlike swimming. *Annu. Rev. Fluid Mech.* **32**, 33–53.

Tseng, Y.-H. & Ferziger, J. H. 2004 Large-eddy simulation of turbulent wavy boundary flow – illustration of vortex dynamics. *J. Turbul.* **5**, 034.

Ursell, F. 1956 Wave generation by wind. In *Surveys in Mechanics* (ed. G. K. Batchelor), pp. 216–249. Cambridge University Press.

Veron, F., Saxena, G. & Misra, S. K. 2007 Measurements of the viscous tangential stress in the airflow above wind waves. *Geophys. Res. Lett.* **34**, L19603.

Wan, F., Porté-Agel, F. & Stoll, R. 2007 Evaluation of dynamic subgrid-scale models in large-eddy simulations of neutral turbulent flow over a two-dimensional sinusoidal hill. *Atmos. Environ.* **41**, 2719–2728.

Wu, J. 1973 Prediction of near-surface drift currents from wind velocity. *J. Hydraul. Div. ASCE* **99**, 1291–1302.

Yang, D. & Shen, L. 2009 Characteristics of coherent vortical structures in turbulent flows over progressive surface waves. *Phys. Fluids*. **21**, 125106.

Zedler, E. A. & Street, R. J. 2001 Large-eddy simulation of sediment transport: currents over ripples. *J. Hydraul. Res.* **127**, 444–452.

Zhou, J., Adrian, R. J., Balachandar, S. & Kendall, T. M. 1999 Mechanisms for generating coherent packets of hairpin vortices in channel flow. *J. Fluid Mech.* **387**, 353–396.